# Saharan dust transport and boundary layer entrainment over Western Europe: multi-instrument observations and convection-permitting model evaluation

Hengheng Zhang[1], Gholam Ali Hoshyaripour[1], Heike Vogel[1*], Frank Wagner[2], Thomas Leisner[1], Jochen Förstner[2], Prabhakar Shrestha[2], and Harald Saathoff[1]

[1]Institute of Meteorology and Climate Research, Karlsruhe Institute of Technology, Eggenstein-Leopoldshafen, Karlsruhe, Germany
[2]Deutscher Wetterdienst (DWD), Frankfurter Str. 135, 63067 Offenbach am Main, Germany
[1]* Retired

**Correspondence:** Hengheng Zhang (zhang@riam.kyushu-u.ac.jp) and Harald Saathoff (Harald.Saathoff@kit.edu)

**Abstract.** Long-range Saharan dust transport affects radiation, clouds, and air quality, yet its vertical structure and entrainment into the boundary layer remain challenging to simulate. We investigate four contrasting dust events over southwestern Germany using ground-based lidar, sun-photometer and in situ aerosol measurements, satellite observations, backward trajectories, and ICON-ART simulations. The events represent diverse atmospheric conditions, including a six-day cloud-free episode, a cloudy episode involving dust–cloud interactions, and an intense outbreak with aerosol optical depth approaching 1.4. A depolarization-based lidar method separated dust backscatter from contributions by other aerosols, enabling a like-for-like evaluation of the dust represented by ICON-ART and providing a useful approach for evaluating dust models in mixed aerosol layers. ICON-ART reproduced the large-scale transport and arrival of the dust layers, with mean differences of approximately 20 min in arrival time and 50 m in layer height. Daily re-initialization of the global simulations improved correlations with observed near-surface particulate matter concentrations from 0.65–0.69 to 0.86–0.88 and better reproduced the timing and persistence of boundary-layer dust. The high resolution runs (2, 1 km) resolved dust-layer stratification, vertical gradients, and exchange between the free troposphere and boundary layer more realistically. However, ICON-ART consistently overestimated particles of 0.5–2 $\mu$m and underestimated particles larger than 2 $\mu$m. These results demonstrate the complementary benefits of accurate meteorological initialization and convection-permitting resolution while identifying size-dependent emission, sedimentation, and deposition as priorities for model development. By distinguishing errors in dust transport from those arising from aerosol size representation, this study provides an observation-constrained framework for evaluating and improving convection-permitting dust forecasts.

## 1 Introduction

The Saharan desert is the largest source of aeolian dust in the world, with annual production rates of about 4 - 7 x $10^8$ tons/year, which is almost half of all aeolian dust inputs to the oceans (Middleton and Goudie, 2001). Saharan dust is mainly produced by natural processes such as wind storms and doesn't appear to be heavily impacted by human activities (Kandler et al., 2007).

Saharan dust has been found to be transported in the free troposphere over long distances reaching e.g.the Amazon basin, middle and north America, Europe (Guerzoni and Chester, 1996), even Japan (Tanaka et al., 2005), and other regions. The Saharan dust impacts ecosystems and human life in the following ways. Firstly, dust impacts ecosystems in various regions like the Atlantic Ocean, the Amazon basin, the southeastern United States, or the Caribbean by providing nutrients such as phosphorus or iron, and in some cases promoting soil development (Molinaroli et al., 1993). Secondly, Saharan dust has also impact on power supply by changing photovoltaic output. When it comes to Saharan dust outbreaks, the photovoltaic output is reduced not only through a significant increase in aerosol optical thickness, but also through dust deposition on the photovoltaic modules on subsequent days (Conceição et al., 2018; Rieger et al., 2017a). Thirdly, Saharan dust particles can also act as cloud condensation nuclei (CCN) or ice-nucleating particles (INP), influencing cloud formation and thereby altering radiative forcing through aerosol indirect effects (Seifert et al., 2023). Finally, Saharan dust outbreaks has impact on short-range weather forecast errors as current weather prediction models still struggle to reproduce cloudiness and radiative effects during dust events, largely because of missing or simplified representations of aerosol–cloud interactions, especially the indirect effects of dust (Hermes et al., 2024).

Changes in circulation patterns associated with climate change have led to an increase in frequency and intensity of Saharan dust events in the Carpathian Basin (Varga, 2020). The annual number of dust events was 4.2 on average between 1979 and 2010, while in the period of 2011–2018, it has increased to 10.3. And an average of about 33,000 tons of atmospheric dust was transported to Central Europe each year from 2002–2017 (Rostási et al., 2022). The increased frequency and amount of Sahran dust loading have caused larger uncertainties in global radiative forcing (Saidou Chaibou et al., 2020; Diop et al., 2020; Mallet et al., 2009).

The predictions of SAL regarding dust arrival time, dust height and structure, as well as dust impact on clouds, precipitation, and convective systems is becoming more important. In past decades, different transport models were developed to simulate the distribution and evolution of aerosol over the globe. For example, the general circulation model the ECHAM-HAMMOZ (Pozzoli et al., 2008a, b), the ECHAM/MESSy Atmospheric Chemistry (EMAC) (Roeckner et al., 2006; Jöckel et al., 2006, 2010), the Whole Atmosphere Community Climate Model (WACCM) (Kunz et al., 2011; Smith et al., 2011), the Weather Research and Forecasting (WRF) model coupled with Chemistry (WRF/Chem) (Chapman et al., 2009), the CONsortium for small-scale MOdeling (COSMO) and its extension on Aerosol and Reactive Trace gases (ART) (Vogel et al., 2014), and its successor the ICOsahedral Nonhydrostatic (ICON) and its extension on Aerosol and Reactive Trace gases (ART) (Hoshyaripour et al., 2026; Rieger et al., 2015; Weimer et al., 2017). A multi-model forecast comparison is now also available by the Sand and Dust Storm Warning Advisory and Assessment System (Benincasa, 2023), a program of the World Meteorological Organization (WMO). The Dust-DN (Dust Doctoral Network) project, an EU-funded initiative under the Horizon Europe program, seeks to advance the scientific understanding of mineral dust processes and improve the predictive capabilities of online coupled chemistry transport models (https://dust-dn.cyi.ac.cy/, last access: 26 December 2024).

Different online coupled chemistry transport models need to be evaluated against a range of measurement methods, including both remote sensing and in-situ observations. This comparison is essential for validating model performance, assessing the validity of parameterizations used in the models, and improving our understanding of aerosol properties and processes during

dust events (Zhang et al., 2022; Hoshyaripour et al., 2019). For example, aerosol lidar is a useful tool to validate Saharan dust model simulations as it can provide high-resolution vertical profiles of SALs (Chouza et al., 2016; Zhang et al., 2022). Ground-based lidar networks including the European Aerosol Research Lidar Network (EARLINET) (Mona et al., 2014), the Micro-Pulse Lidar Network (MPLNET) (Misra et al., 2012), and the Asian Dust and Aerosol Lidar Observation Network (AD-Net) (Sugimoto et al., 2016) have conducted long-term dust observation in last decades to investigate dust transport and optical proprieties. Also the sun photometers deployed by the Aerosol Robotic Network (AERONET) (Kim et al., 2011) provides rich information on column integrated dust optical parameters (e.g. Aerosol optical depth (AOD), Ångström Exponent (AE), single scattering albedo (SSA)). Finally, satellite data can be also used to study Saharan dust proprieties and validate online coupled chemistry transport model. For example, the MODIS instrument aboard the Terra & Aqua satellites can provide column integrated aerosol optical properties (Merdji et al., 2023; Barnaba and Gobbi, 2004) and the Cloud-Aerosol Lidar with Orthogonal Polarization (CALIOP) aboard of the CALIPSO satellite can provide vertical profiles of aerosol information (Hoshyaripour et al., 2019; Liu et al., 2008). The valuable satellite data provided by these active or passive remote sensing sensors aboard different satellites help to understand the dust proprieties over the globe (Song et al., 2022; Wu et al., 2020).

Central Europe, provides an excellent location for investigating SALs. Firstly, this region is frequently affected by long-range transported Saharan dust events, especially during spring and summer seasons (Ansmann et al., 2003; Gasteiger et al., 2011). Second, the typical transport time for dust particles—ranging from 2 to 5 days—makes it ideal for examining long-range dust transport and its interactions with local atmospheric conditions (Ansmann et al., 2003). Additionally, the region's diverse meteorological patterns, including extreme weather events such as storms and prolonged dry periods, play a significant role in dust movement and deposition, offering a wide range of scenarios for analysis (Kunz et al., 2022a). These factors make southwest Germany a key site for validating global transport models, with insights gained here being broadly applicable to other regions with similar characteristics.

Zhang et al. (2022) investigated the properties and transport of Saharan dust during the period from $7^{th}$ to $9^{th}$ April 2018, through a synergistic approach combining modeling and observational data. They demonstrated that a novel method for retrieving the lidar ratio from scanning aerosol lidar measurements could be effectively applied to the SAL, yielding optical parameters (e.g., lidar ratio and particle depolarization ratio) consistent with values reported in the literature. Their study also showed that the modeled backscatter coefficients agreed well with lidar observations when non-spherical particles were assumed, with a slope of $0.9 \pm 0.1$ ($R^2 = 0.68$). In contrast, assuming spherical particles led to a significant overestimation, with a slope of $2.3 \pm 0.3$ ($R^2 = 0.74$). In the present study, we utilize a more comprehensive dataset to investigate the evolution and optical properties of dust in southwest Germany, extending the analysis to a broader set of dust events and characteristics. A scanning aerosol lidar systems, a sun photometer, different ground-level in-situ aerosol characterisation instruments (e.g. Optical Particle counter (OPC)), the CALIPSO, the MODIS, and a online coupled aerosol and chemistry transport model, ICON-ART model (Hoshyaripour et al., 2026), were employed in 4 Saharan dust cases to investigate these dust events employing different retrieval methods. Three of these events are discussed in detail in this study. Case 1 was previously examined by Zhang et al. (2022), but it is also included here in the statistical analysis. The objectives of this study are to (1) characterize the transport pathways, vertical structure, optical properties, and size distributions of Saharan dust using a unique combination

of ground-based, in-situ, and satellite observations; (2) evaluate the ability of ICON-ART to reproduce these observed dust characteristics; and (3) investigate the influence of model resolution and meteorological initialization on the representation of long-range transported Saharan dust over Europe.

This paper is organised as follows. Section 2 describes the remote sensing and in situ methods as well as the model simulations. Details of the dust observations and dust properties are discussed in section 3 including a comparison of the different remote sensing and in situ methods as well as how they compare to the model predictions. In the final section, we provide some conclusions.

## 2 Method

Four Saharan dust events were investigated combining remote sensing, ground-level in situ measurements, and ICON-ART model over western Europe. The four selected cases were chosen to sample a broad range of aerosol and cloud conditions. Case 1 was detailed discussed by Zhang et al. (2022). Case 2 corresponds to the longest cloud-free Saharan dust episode, lasting approximately six days, and serves as a reference case for examining the temporal evolution and vertical structure of SALs under clear-sky conditions. Case 3 documents the interaction between Saharan dust and clouds, allowing an investigation of dust–cloud coupling processes and their influence on observed vertical structures. Case 4 represents the most intense dust outbreak, with aerosol optical depth (AOD) approaching 1.4, and is used to assess the vertical distribution and optical characteristics of extremely dense dust layers. Together, these cases provide a comprehensive framework for evaluating lidar observation strategies and for characterizing Saharan dust under diverse atmospheric conditions. A scanning aerosol lidar (Zhang et al., 2022) provided spatial-temporal distributions of SALs and optical proprieties of dust particles. Also, a sun photometer (Giles et al., 2019) provided wavelength-dependent aerosol optical depth (AOD), Angstrom exponent (AE), and under clear sky conditions the aerosol size distributions (ASD), and single scattering albedo (SSA). Besides, ground-level in situ aerosol characterisation instruments (e.g. OPC, APS, SMPS, and CPC) provided aerosol number concentration and mass concentration as well as aerosol size distribution. Finally, these observational data were compared with forecasts from ICON-ART (Hoshyaripour et al., 2026). The model is running in operational mode by Deutscher Wetterdienst (DWD) since March 2024. The main methods used to characterize the four different Saharan dust events are summarized in Table 1.

### 2.1 Remote sensing methods

Karlsruhe scanning aerosol lidar (KASCAL (LR111-ESS-D200, Raymetrics Inc.)) was deployed at the campus north of the Karlsruhe Institute of Technology (8.4298° E, 49.0953° N, 119 m above sea level) during the dust event of April 2018, February 2021, and March 2022. It was deployed in Rottenburg am Neckar (8.95452° E, 48.4892° N, 339 m above sea level) for dust events that occurred on June 2021 (Kunz et al., 2022b). The KASCAL lidar system is a mobile scanning system with an emission wavelength of 355 nm. The laser head, 200 mm telescope, and lidar signal detection units are mounted on a rotating platform. The overlap range of the lidar system is 255 m and the overlap correction for the KASCAL lidar has been done with horizontal measurements assuming horizontal homogeneous conditions. The KASCAL lidar operates automatically

**Table 1.** List of available ground/satellite observations and model forecasts for the Saharan dust events (SPH[a]: Sun photometer; KIT-CN[b]: KIT campus north). *Please note that the dust particles didn't reach ground level during events 1 & 4 so that no in situ measurements could be conducted.

| ID | Date | Observation site | lidar | OPC | APS | SPH[a] | ICON-ART |
|---|---|---|---|---|---|---|---|
| 1 | $7^{th}$-$9^{th}$ April 2018 | KIT-CN [b], (8.4298° E, 49.0953° N) | X | | | X | X ($\Delta$ = 26 km) |
| 2 | $22^{nd}$ - $27^{th}$ February 2021 | KIT-CN, (8.4298° E, 49.0953° N) | X | X | X | X | X ($\Delta$ = 26, 13, 2, 1 km) |
| 3 | $19^{th}$-$20^{th}$ June 2021 | Rottenburg, (8.95452° E, 48.4892° N) | X | X | X | X | X ($\Delta$ = 26 km) |
| 4 | $16^{th}$-$22^{nd}$ March 2022 | KIT-CN, (8.4298° E, 49.0953° N) | X | | | X | X ($\Delta$ = 26 km) |

and continuously according to a predefined schedule using software developed by Raymetrics Inc.a software developed by Raymetrics Inc. (Avdikos, 2015). For the data analysis and calibration of the system, we followed the quality standards of the European Aerosol Research Lidar Network (EARLINET) (Freudenthaler, 2016; Zhang et al., 2022).

Tesche et al. (2009b) proposed a method to separate the total backscatter coefficient into a dust part and a non-dust part using the following equation:

$$\beta_{\lambda,d} = \beta_{\lambda,p} \frac{(\delta_{\lambda,p} - \delta_{\lambda,nd})(1 + \delta_{\lambda,d})}{(\delta_{\lambda,d} - \delta_{\lambda,nd})(1 + \delta_{\lambda,p})} \tag{1}$$

Where $\beta_{\lambda,d}$ is the pure dust backscatter coefficient, $\beta_{\lambda,p}$ is the total particle backscatter coefficient, $\delta_{\lambda,p}$ is the total particle depolarization ratio, $\delta_{\lambda,nd}$ is the particle depolarization ratio of non-dust particles, $\delta_{\lambda,d}$ is the particle depolarization ratio of the pure dust particle. In this equation, $\beta_{\lambda,p}$ and $\delta_{\lambda,p}$ can be retrieved from lidar measurement.

The sun photometer (CE-318, CIMEL, Holben et al. (1998)) which measures solar radiance at nine different wavelengths ranging from 339 nm to 1638 nm was also deployed in these four Saharan dust events. The sun photometer data enables calculation of AOD at specific wavelengths. Additionally, the data can be used to determine other important aerosol parameters such as (Single Scattering Albedo (SSA), Ångström Exponent (AE), (Aerosol Size Distribution(ASD, and complex refractive index (CRI) (Vermeulen et al., 2000; Sinyuk et al., 2020; Dubovik and King, 2000). SSA measures the ratio of scattering coefficient to extinction coefficient, which is inversely proportional to the aerosol absorption ability. AE describes the wavelength dependency of AOD, which is influenced by particle size. Smaller particles exhibit a stronger wavelength dependency, resulting in a higher AE value. Additionally, clear sky measurements from the sun photometer can be used to derive ASD (between 0.05 – 15 $\mu$m), complex refractive index (between 1.33 – 1.6 and 0.0005i – 0.5i), and other parameters (Dubovik and King, 2000; Müller et al., 2010). The sun photometer is part of the Aerosol Robotic Network (AERONET) and level 2.0 data was utilized in this study (Giles et al., 2019).

## 2.2 Ground-level in-situ instruments

The ground-level in-situ instruments were deployed in a mobile container for the field campaign at Rottenburg am Neckar and were installed in the laboratory of building 322 on campus north of the KIT near the village of Eggebstein-Leopoldshafen. Aerosol particle size distributions were measured using scanning mobility particle sizer (SMPS; DMA: TSI 3080, CPC 3022A, TSI Inc., 14-760 nm), aerodynamic particle sizer (APS; TSI 3321, TSI Inc, 0.5 - 20 $\mu$m), and optical particle counter (OPC; Fidas200, Palas, GmbH, 0.18 - 18 $\mu$m). Additionally, two condensation particle counters (CPC3776, 3025, TSI Inc.) were used for counting particle numbers (>2.5 nm) with a time resolution of 1 second. These instruments operated with a flow rate of 5 L/min and a time resolution of 1-5 minutes during Saharan dust events 2 and 3. Additionally, two condensation particle counters (CPC3776, 3025, TSI Inc.) were used to count particle numbers with a time resolution of 1 second. Meteorological parameters were measured using a compact sensor (WS7000, Luff) (Jiang et al., 2025).

## 2.3 ICON-ART data and simulations

To predict the transport and distribution of dust during the four Saharan dust events, the ICON-ART model system was used. ICON-ART is an online-coupled chemistry transport modelling system that combines numerical weather prediction and climate modelling with the representation of aerosols and trace gases, including their life cycle and interactions with radiation and clouds (Hoshyaripour et al., 2019). The ICON model solves the fully compressible, non-hydrostatic three-dimensional Navier–Stokes equations on an icosahedral grid (Zängl et al., 2015), while the ART extension includes aerosol and trace gas processes (Hoshyaripour et al., 2026). In this study ICON-ART only simulates the mineral dust with radiation coupling. However, the indirect effect is not simulated in the results presented here. ICON-ART predicts mass and number mixing ratio of mineral dust for three modes which are assumed to be lognormally distributed with fixed standard deviation. The median diameter is a diagnostic variable with mass median diameters of 1.5, 6.7, and 14.2 µm, and geometric standard deviations of 1.7, 1.6, and 1.5, respectively. Dust emissions are parameterized following Vogel et al. (2006) and Rieger et al. (2017b), accounting for soil properties, soil aggregation state, and soil-type heterogeneity. The model further considers major dust removal processes, including sedimentation as well as dry and wet deposition. The Aerosol Optical Depth (AOD) and backscatter coefficients are diagnosed at 550 nm and 532 nm respectively, assuming non-sphericity of the dust particles(Hoshyaripour et al., 2019).

The ICON-ART data used in this study originate from two different model configurations. For the baseline analysis of the four measurement campaigns, forecast data were obtained from the quasi-operational dust forecasting system of the Deutscher Wetterdienst (DWD). The forecasting system consists of a global domain coupled to a regional nest over North Africa and Europe, with horizontal resolutions of 40 and 20 km, respectively. The model employs 65 vertical layers, with layer thickness increasing from near surface layer height of 10 m to several kilometers in the upper atmosphere. In the altitude range between 2 and 6 km, where long-range transported dust layers are frequently observed, the vertical resolution is approximately 200–400 m.

For the February 2021 case study, dedicated high-resolution ICON-ART simulations were performed specifically for this study using the regional limited-area mode (LAM) configuration with an additional nested domain, employing horizontal resolutions

of 2 and 1 km, respectively. The lateral boundary conditions for the LAM simulations were provided by a 13 km European domain embedded within a 26 km global domain. This high-resolution setup was designed to better resolve mesoscale processes and to investigate the causes of discrepancies between simulations and observations in greater detail. We used the quasi-operational global ICON experiments with mineral dust at 40 km resolution available from the DWD servers to generate the initialized analysis at current operational global (ICON) and nested grid (ICON-NA2: North Africa North Atlantic) at 26 km and 13 km, respectively. Here, it has to be noted that the analysis is only available for the meteorological variables, while no analysis exists for the dust tracers. So, an error source based on the model parameterization of dust emission, deposition remains. We acknowledge this important short-coming for modelled dust in the study. Nevertheless, the model provides valuable information about the spatial transport of dust at high resolution from the Saharan desert to Europe. Using the initialized analysis on 12:00 on $21^{st}$ February 2021, we make a 5 day forecast run (EXP-5d). For limited area mode (LAM) runs at higher resolution over Germany (ICON-D2: 2 km) with nest over Alpine region (ICON-A1: 1 km), we remap the initialized analysis to LAM grids and use the hourly boundary conditions from EU-NA2 nest for the 5 day forecast. In addition, we also conducted a 24 hour forecast run with the Global runs using re-initialization at 12:00 for the same 5 day period (RI-EXP-1d). The re-initialization is again based on the archived global ICON experiments at 40 km resolution. For the LAM runs, we use the initial conditions on $21^{th}$ February 2021 and make a 5 day forecast run using the updated lateral boundary condition files from re-initialized global runs with nest.

## 3 Results

To investigate the dominant physical processes controlling Saharan dust transport over Western Europe, Four representative meteorological scenarios are analyzed combining remote sensing, in situ measurements, and ICON-ART model calculations. The transport of the four SALs were first investigated by the HYbrid Single-Particle Lagrangian Integrated Trajectory (HYSPLIT) model. The hourly seven-day backward trajectories were calculated during Saharan dust periods for altitudes from 500 to 7500 m with an interval of 1000 m based on the HYSPLIT model. The frequency of these trajectories at two altitudes levels (Low altitude: 500 m & High altitude: 1500 m - 7500 m) is shown in Figure 1. The reasons for classifying these trajectories into two groups is that the trajectories at an altitude of 500 m are related to the transport of aerosol within the boundary layer while the high-altitude (1500 - 7500 m) ones are related to the long-distance transport in the free troposphere. The frequency map of high altitude trajectories shown at the bottom of Figure 1 indicates that most of the trajectories originated from north Africa (Sahara Desert) as expected. However, the places of origin are different at low-altitude for these 4 Saharan dust cases. In case 1, most of the air parcel trajectories originated over the Atlantic Ocean, indicating that sea salt aerosols were likely transported over a long distance from the ocean to the study area by prevailing winds. During case 2, most of the low-altitude trajectories also originated from north Africa (Sahara Desert), which is the reason why the Saharan dust particles could be measured by ground in situ instruments during this case. During case 3 and case 4, the low-altitude trajectories are of local origin, which is related to the transport of local aerosol.

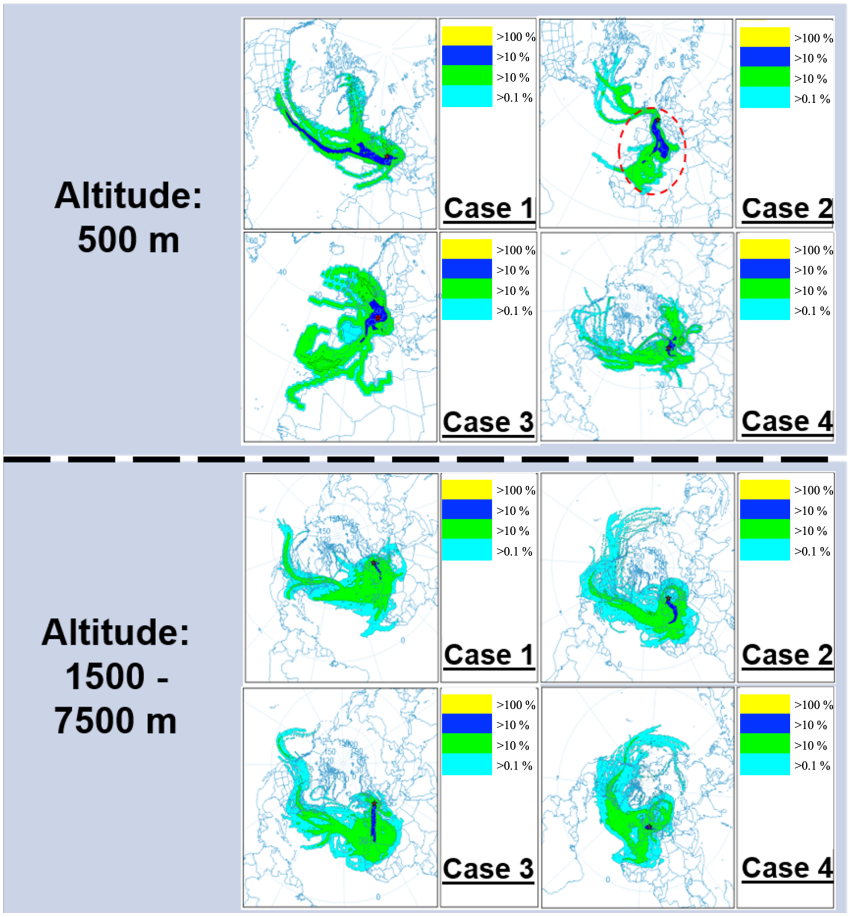



**Figure 1.** Frequency of trajectories at two altitude levels (500 m and 1500 - 7500 m) during four Saharan dust case periods based on back trajectories calculated by the HYbrid Single-Particle Lagrangian Integrated Trajectory (HYSPLIT) model. (The case IDs are labeled in Table 1)

### 3.1 Evolution of Saharan dust events under different meteorological conditions

#### 3.1.1 Long-lasting cloud-free dust event (Case 2)

There were 3 separate dust events observed from KIT Campus north (north of Karlsruhe city) in Feb 2021, but we will focus only on the dust event from $22^{nd}$ to $26^{th}$ February, which lasted for almost 5 days. This period was generally free of clouds. Figure S2 displays the horizontal distributions of daily averaged aerosol optical depth (AOD) from MODIS satellite measurements with a spatial resolution of $0.4° \times 0.4°$, for the period from $22^{nd}$ to $26^{th}$ February 2021. The data reveal that during this period, Saharan dust originating from North Africa was transported to Karlsruhe, Germany, showing distinct signatures of SALs in the atmosphere. Figure 2 shows the time series of backscatter coefficients from KASCAL measurements, ICON-ART predicted backscatter coefficients, Linear Volume Depolarization Ratio (LVDR) and Linear Particle Depolarization Ratio (LPDR) from

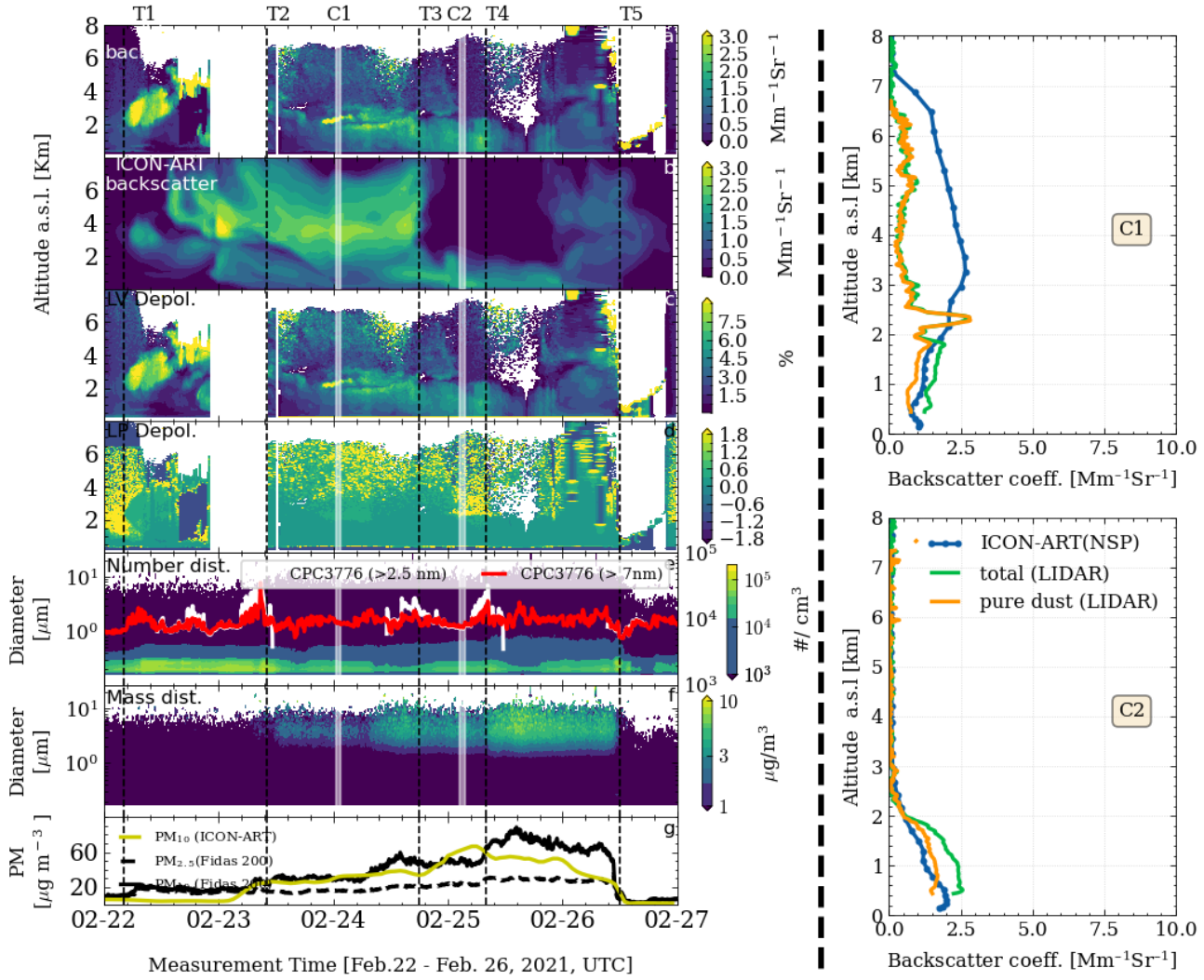



**Figure 2.** Time series of backscatter coefficients from KASCAL measurements (a), predicted backscatter coefficients by ICON-ART (b), Linear Volume Depolarization Ratio (LVDR) (c) Linear Particle Depolarization Ratio (LPDR) (d) from KASCAL measurements, particle number size distribution from Fidas 200 and particle number concentration from two CPCs (e), particle mass size distribution from Fidas 200 (f) and particulate matter concentrations ($PM_{10}$ & $PM_{2.5}$ ) from the Fidas 200 and the lowest model level (150 m) of the ICON-ART simulation (g) from $22^{nd}$ to $26^{th}$ February 2021 for case 2. The profiles of backscatter coefficients measured by the lidar and predicted by ICON-ART model for case C1 (Averaged profiles from 00:30 to 1:30 for lidar measurement and profile at 01:00 for ICON-ART prediction on $24^{th}$ February 2021) and for a selected time C2 (Averaged profiles from 02:30 to 03:30 for lidar measurement and profile at 03:00 for ICON-ART prediction on $25^{th}$ February 2021) are shown on the right side of this figure. The vertical dashed lines in the contour plots indicate dust arrival (T1), dust touched to the ground (T2), an increase of PM concentration at ground level (T3 & T4) and a low-level cloud appeared (T5). C1 and C2 represent time periods used for a more detailed data analysis as shown in the right side of this figure.

KASCAL measurements, particle number size distributions and particle number concentration from two CPCs, particle mass size distributions and particle matter concentrations from OPC (Fidas200) measurements from $22^{nd}$ to $26^{th}$ February 2021. As can be seen from this figure, the dust arrived at the observation site at 04:00 on $22^{nd}$ February 2021 (dashed line T1) and lasted for about 5 days. Initially, the SAL had a maximum backscatter at around 2.0 km altitude, and then the SAL started sinking and reached ground level at 10:00 on $23^{rd}$ February 2021 (dashed line T2), and these ground level particles were characterized by an in situ aerosol sizer (Fidas200). Subsequently, the ground level aerosol concentration increased stepwise as can be seen from the mass size distributions (Figure 2f) and particle mass concentrations (Figure 2g) from 12:00 on $24^{th}$ February 2021 to 12:00 on $26^{th}$ February 2021. However, the increase in particle number concentration is not obvious in Figure 2e, because the aerosol number concentration is dominated by smaller particles. Finally, a sharp decrease of ground level aerosol dust particles and dust concentration at high altitudes can be seen from both, ground level in situ and lidar measurements at 12:00 on $26^{th}$ February 2021 (dashed line T5) due to increasing wind speeds advecting clean air masses.

The evolution of the SAL over Karlsruhe for dust case 2 predicted by the ICON-ART model is shown in Figure 2b. According to the model simulation, the SAL arrived in Karlsruhe at 04:00 on $22^{nd}$ February 2021, and lasted for about five days. Initially, the ICON-ART predicted dust backscatter ranged between 1.0 and 8.0 km. Subsequently, the higher-altitude (3-8 km) SAL clears out after 18:00 on $24^{th}$ February 2021 while the lower level (<3 km) dust backscatter continually increases towards the ground level. The time series of particulate mass concentrations ($PM_{10}$) from Fidas measurements and dust mass concentration from the ICON-ART simulation, shown in Figure 2g, reveal a good correlation of $PM_{10}$ between Fidas 200 measurement and ICON-ART prediction, with a slope of $0.754 \pm 0.041$ and a Pearson correlation coefficient of 0.862, indicating the a relative good performance of the ICON-ART prediction. The dust layer heights and their peak heights for both lidar measurement and ICON-ART prediction are shown in Figure 8b. The dust peak heights are not shown after 18:00 on $24^{th}$ February 2021 for lidar measurement due to the influence of boundary layer aerosol loading during this time and boundary layer aerosol having maximum values near ground level. The vertical profiles of total and pure backscatter coefficients from lidar measurements and ICON-ART calculations are shown at the right of Figure 2 for two selected periods indicated as C1 and C2 in Figure 2. For case C1, the backscatter coefficients are averaged from 00:30 to 01:30 for lidar measurements and ICON-ART simulation is sampled at 01:00 on $24^{th}$ February and for case C2, the backscatter coefficients are given as average of lidar measurements between 02:30 to 03:30 and ICON-ART calculations for 03:00 on $25^{th}$ February 2021. As can be seen in the vertical profiles for the C2 period, the boundary layer aerosol and dust particles are mixed below 2.0 km and this mixing requires additional analysis to determine dust peak heights from lidar measurements. In addition, the ICON-ART shows relatively larger backscatter coefficient especially at altitude above 2.8km. Profiles in case C2 show consistencies in dust layer height but inconsistencies in backscatter coefficients. As discussed for Saharan dust case 1, the predicted backscatter coefficients can agree well with values retrieved from lidar measurements if non-spherical particles are assumed (Zhang et al., 2022). However, during period C2 of Saharan dust case 2, the ICON-ART predicted backscatter coefficients were systematically lower than those from lidar retrievals. The main reason for this difference to the backscatter coefficients retrieved from lidar measurements is the contribution of non-dust particles to the total backscatter coefficient in this mixing layer. The comparison of backscatter coefficients from LIDAR measurement with ICON-ART simulation for C2 periods shows that backscatter coefficients predicted by ICON-ART

255 are smaller than the total backscatter coefficients measured by KASCAL by a factor of 2.12 ± 0.66 while it agrees well with the pure dust backscatter coefficient by a factor of 1.06 ± 0.22. This is expected as ICON-ART only simulates mineral dust, but adds confidence for our model results.

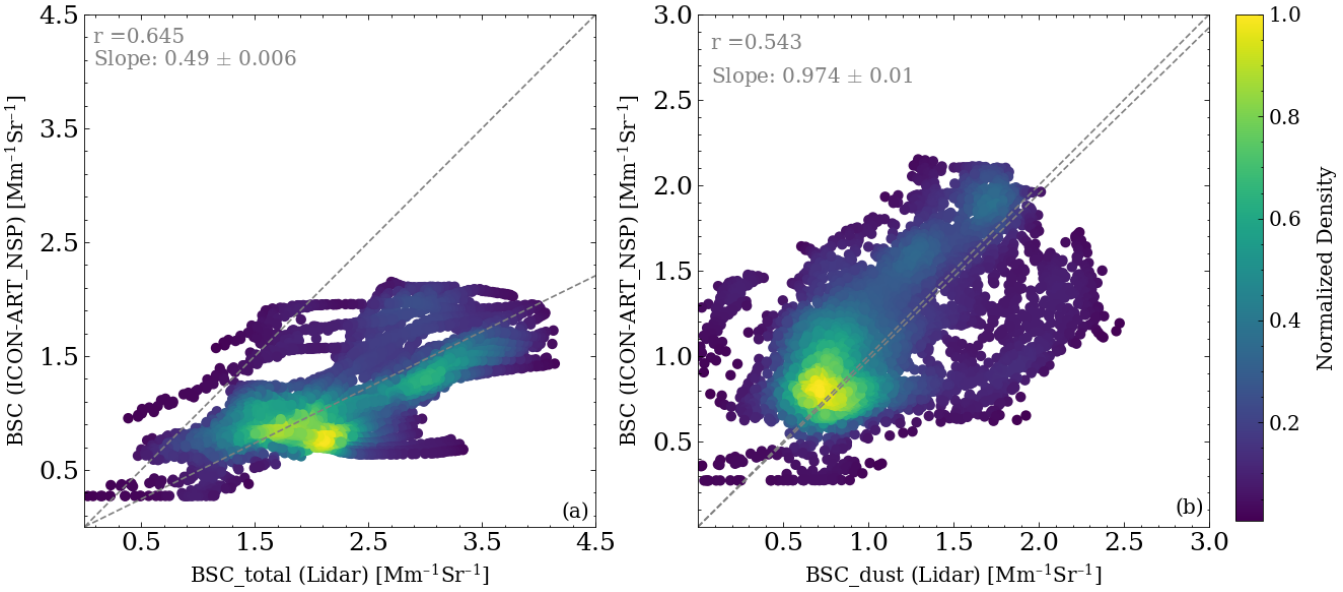



**Figure 3.** Correlation of backscatter coefficients predicted by ICON-ART and those retrieved from KASCAL for both total aerosol particles (a) and dust particles only (b) (from 20:00 on $24^{th}$ to 12:00 to $26^{th}$ February 2021 for Case 2).

Figure 3 shows the correlation of the backscatter coefficient predicted by ICON-ART and those retrieved from KASCAL measurements for both total aerosol particles (left) and dust particles only (right). This correlation only shows the data from 20:00
260 on $24^{th}$ to 12:00 on $26^{th}$, February 2021 as backscatter coefficients are inconsistent between lidar and ICON-ART model before this time. The backscatter coefficients predicted by ICON-ART for dust are systematically lower than the total backscatter coefficient retrieved from lidar data by a factor of 1.94 ± 0.65. However, the pure dust backscatter coefficients retrieved from KASCAL agrees well with the backscatter coefficients predicted by ICON-ART with the a slope of 0.974 ± 0.01 and a Pearson correlation coefficient of 0.543 as shown in Figure 3. From these comparisons, we can see that the signal from non-dust aerosol
265 particles can successfully be separated from total backscatter coefficients, allowing for a comparison between lidar measurements and ICON-ART simulations for the Saharan dust also at lower altitudes. The contribution of non-dust aerosol particles can also be seen from comparison of AOD values from sun photometer measurements with ICON-ART results (cf. Figure S3).

Figure 4 shows the time series of AOD (a), AE (b), SSA (c) measured by the sun photometer for different wavelengths as well
270 as column-averaged aerosol volume size distributions retrieved from the sun photometer (d) and aerosol mass size distributions measured by Fidas200 at ground level (e). From this figure, we can see a relatively small trend of AOD for different wavelengths

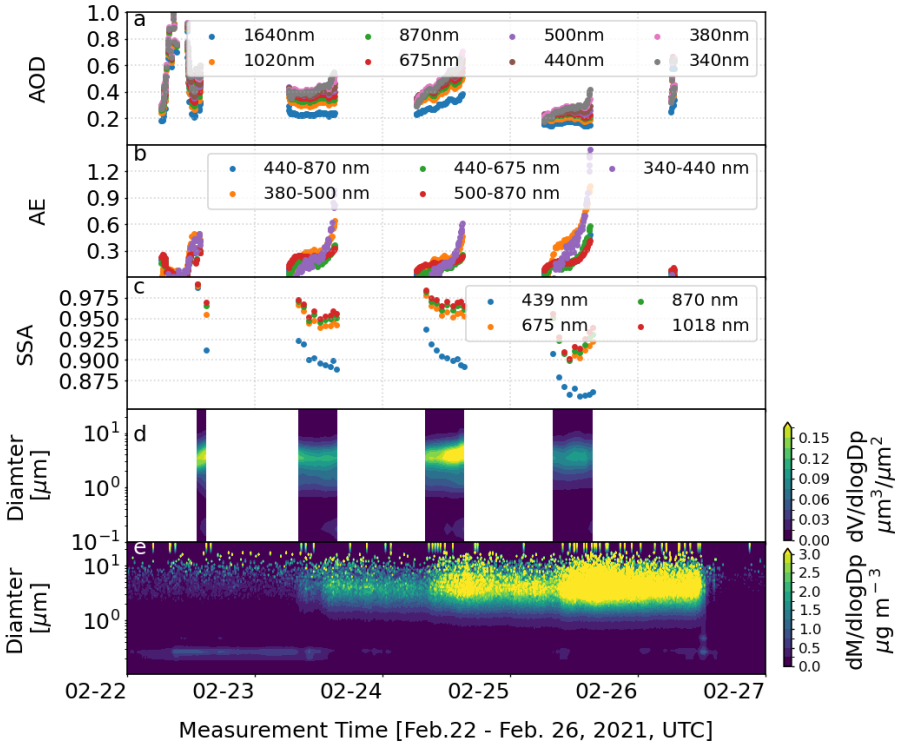



**Figure 4.** Time series of Aeosol Optical Depth (AOD) (a), Ångström Exponent (AE) (b), Single Scattering Albedo (SSA) (c) at different wavelengths, and column-averaged aerosol volume size distribution (d) measured and retrieved from sun photometer (AERONET, Karlsruhe station) as well as particle mass size distributions (e) measured by Fidas 200 from $22^{nd}$ to $26^{th}$ February 2021 for case 2.

caused by large Saharan dust particles over Karlsruhe. These large particles have only very little wavelength dependence in light scattering, thus causing a low value of AE which is below 0.3 most of the time. In addition, the AOD at the wavelength of 340 nm increased from 0.41 at 07:22 on $23^{rd}$ February to 0.66 at 15:57 on $24^{th}$ February 2021 and then decreased to 0.42 at 16:00 on $25^{th}$ February 2021. The SSA shown in panel (c) of this figure indicates that the SSA is wavelength dependent and has the lowest value at a wavelength of 439 nm. This phenomenon is due to the strong absorption of Saharan dust at short wavelengths and this strong absorption caused a low value of SSA. The column-averaged aerosol volume size distribution retrieved from sun photometer and mass size distributions measured by Fidas200 shown in panel (d) and panel (e) show relatively large particles ($d_p > 1$ $\mu$m) dominating during this Saharan dust period as expected. In addition, the column-averaged volume size distribution retrieved from sun photometer and the mass size distributions from Fidas200 do not show a similar trend. The sun-photometer-retrieved aerosol volume concentration reached its maximum on $24^{th}$ February 2021, whereas the surface aerosol mass concentration measured by Fidas200 peaked on $25^{th}$ February 2021. The one-day difference likely reflects the different measurement principles and sampling volumes of the two instruments. The reason for this inconsistency can be explained as

follow: (1) The sun photometer measures the column integral aerosol from ground level to the tropopause while the Fidas200 measured ground level aerosols. (2) the Saharan dust has the strongest intensity on $24^{th}$ February 2021 (as can be seen from AOD value at panel(a)) but most dust particles are aloft (can be seen from lidar measurement shown in the 2a) which cannot be measured by Fidas200 but can be measured by sun photometer. However, on $25^{th}$ February, most of the dust particles were sunken to the ground level (as can also be seen from lidar measurement shown in Figure 2a) which were measured by Fidas200. In addition, as the SAL mass loading on $25^{th}$ February 2021 is weaker than that on $24^{th}$ February 2021, the column-averaged volume size distribution retrieved by sun photometer for the column average is lower on $25^{th}$ February 2021.

The time series of total and coarse mode AODs from sun photometer measurements at 500 nm and AOD from ICON-ART model simulations at 550 nm between $22^{nd}$ February and $26^{th}$ February 2021 are shown in Figure S3. This time series is divided into three periods (A, B, C) as shown in figure S3 for discussion below. For period A and C, the coarse mode AOD measured by the sun photometer is systematically larger than that predicted from ICON-ART by a factor of 2.03 $\pm$ 1.34. However, during period B, the AOD from ICON-ART is larger than that measured by the sun photometer by a factor of 1.98 $\pm$ 0.28. The reasons for this discrepancy can be explained by the synoptic conditions of the event. During Period A ($22^{nd}$–$23^{rd}$ February), a strong dust surge associated with a cold front and warm conveyor belt transport led to a rapid AOD increase. ICON-ART underestimates the AOD peak observed by the sun photometer, particularly at 340 nm, suggesting lower simulated dust loading during the initial uplift and long-range transport phase, possibly low bias in emission. In Period B ($23^{rd}$–$25^{th}$ February), continued dust advection into Central Europe under a stationary Omega block resulted in sustained elevated AOD levels. ICON-ART overestimates AOD during this period, indicating possible differences in vertical mixing and removal processes in the model compared to observations under dry, clear-sky conditions. For Period C ($25^{th}$–$27^{th}$ February), the dust event gradually subsided. Model and observational AOD values show better agreement, though ICON-ART slightly underestimates AOD during.

### 3.1.2 Dust-cloud interaction (Case 3)

The Saharan dust case 3 occurred during the Swabian MOSES campaign from June to August 2021 near the city of Rottenburg in western Germany (Kunz et al., 2022b). During this field campaign, several intensive observation periods (IOPs) were conducted and this Saharan dust case was measured during IOP4. Figure S4 presents the horizontal distribution of daily averaged aerosol optical depth (AOD) derived from MODIS satellite observations at a spatial resolution of 0.4° × 0.4°, for the period of $19^{th}$–$20^{th}$ June 2021. Figure 5 shows the time series of range corrected lidar signals (RCS) for the cross-polarized channel and LVDR from KASCAL measurements. The backscatter coefficient and particle depolarizations are not shown in this figure as the retrievals of the backscatter coefficients by the Klett-Fernald method were largely affected by the presence of clouds and this effect would bring large uncertainties in calculating the backscatter coefficients and LPDR. Figure 5 also shows the time series of ICON-ART predicted backscatter coefficients, the particle number and mass size distribution and particulate matter concentrations from OPC, and meteorological parameters from $19^{th}$ to $20^{th}$ June 2021. As can be seen from this figure, this SAL arrived in Rottenburg at 11:00 on $19^{th}$ June 2021 (dashed line T1) and lasted for nearly 2 days. Initially, the dust layer showed a maximum in volume depolarization ratio at an altitude of 4.0 km which subsequently sunk to an altitude of 2.0 km.

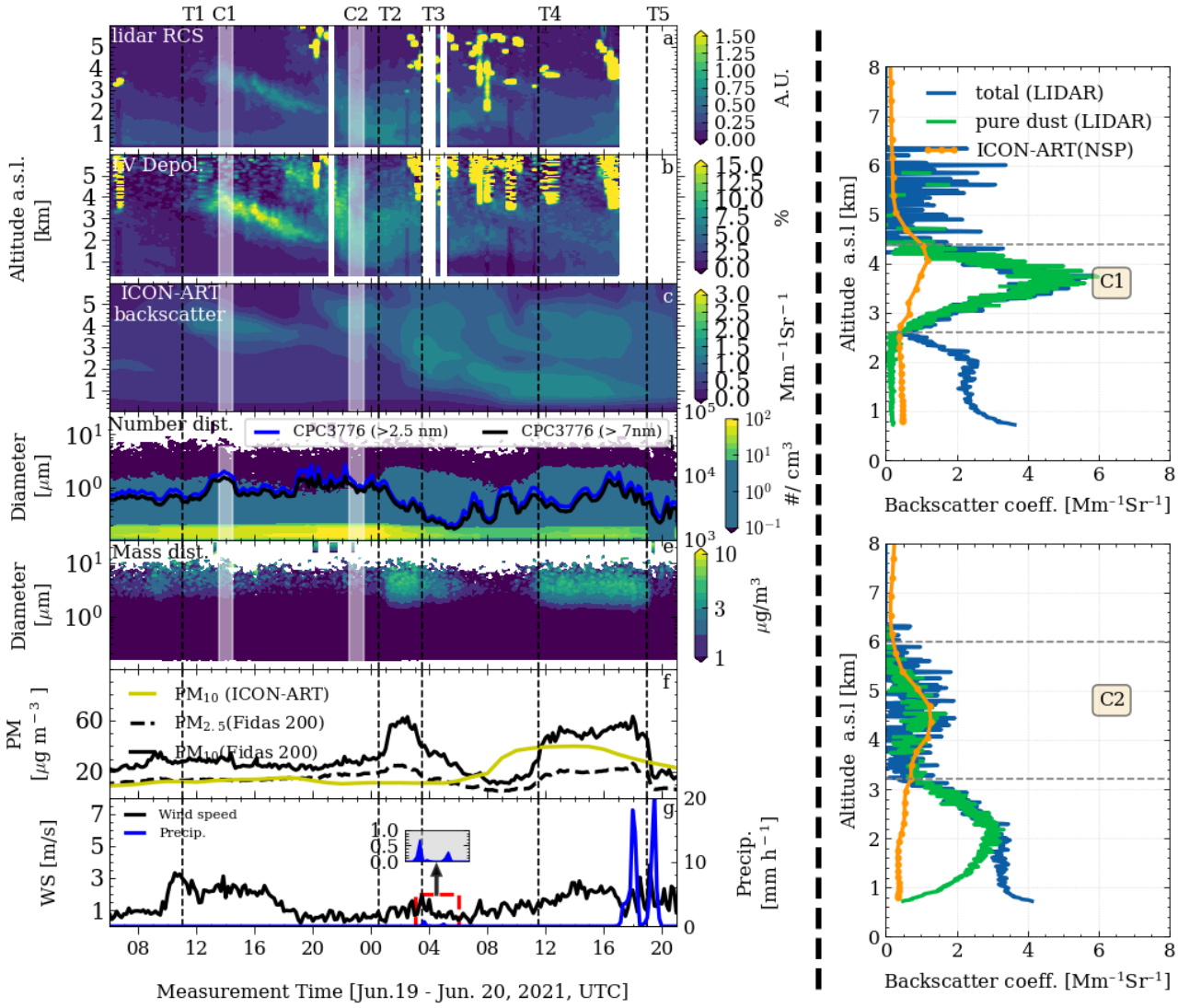



**Figure 5.** Time series of range corrected lidar signal for the cross-polarized channel (a), and Linear Volume Depolarization Ratio (LVDR) from KASCAL measurements (b), backscatter coefficients predicted by ICON-ART (c), particle number size distributions from Fidas 200 and particle number concentration from two CPCs (d), particle mass size distributions from Fidas 200 (e) and particulate matter concentrations ($PM_{10}$) from the Fidas 200 and the lowest model level (150 m) of the ICON-ART simulation (f), and ground level meteorological parameters (e.g. wind, precipitation, WS700) (f) from $19^{th}$ to $20^{th}$ June 2021 for case 3. The profiles of backscatter coefficients measured by the lidar and predicted by the ICON-ART model for case C1 (averaged profiles from 13:30 to 14:30 for lidar measurements and profile at 14:00 for ICON-ART prediction on $19^{th}$ June 2021) and for case C2 (averaged profiles from 22:30 to 23:30 for lidar measurements and profile at 23:00 for ICON-ART prediction on $19^{th}$ June 2021) are shown on the right side of this figure. The vertical dashed lines in the contour plots indicate dust arrival (T1), dust touched to the ground (T2 & T4), and dust particle removal due to precipitation (T3 & T5). C1 and C2 represent time periods used for a more detailed data analysis as shown in the right side of this figure.

At 22:00 on $19^{th}$ June 2021, another dust layer with an initial altitude between 2.0 km to 4.0 km arrived at the observation station then subsequently at lower level after 00:30 on $20^{th}$ June 2021 (dashed line T2). Those particles reaching ground level were characterized by the OPC Fidas200 showing an increase in aerosol concentrations until 03:30 (dashed line T3) on $20^{th}$ June 2021. At 03:00 on $20^{th}$ June 2021, drizzle occurred as shown in panel (g) of this figure and washed the particles out. This caused a decrease of aerosol concentrations measured at ground level. At 11:30 on $20^{th}$ June 2021 (dashed line T4), the aerosol particles reached ground level again and caused an increase of aerosol concentrations at ground level from 11:30 on $20^{th}$ June 2021 to 19:00 on $20^{th}$ June 2021 (dashed line T5). Finally, a moderate rain occurred at around 17:00 on $20^{th}$ June 2021 causing a sharp decrease of aerosol particles (T5) due to wet removal.

The evolution of the SAL over Rottenburg for dust case 3 predicted by the ICON-ART model is shown in Figure 5c. This plot shows a SAL arrival at Rottenburg at 11:00 ($\pm$ 20 min) on $19^{th}$ June 2021 with an initial dust layer height between 4.0 - 5.0 km and lasting for nearly two days. Since 23:30 on $19^{th}$ June 2021, a relative thick dust layer between ground level and up to 6.0 km was over Rottenburg. The dust layer heights and their peak heights for both lidar measurements and ICON-ART predictions for this Saharan dust case are shown in Figure 8c. The dust peak heights from KASCAL after 02:00, $20^{th}$, June 2021 are not shown in this panel as low clouds and precipitation impeded the retrieval of dust peak heights from lidar measurement. This figure shows that the dust layer heights from ICON-ART predictions and lidar measurements show similar trends but still show some discrepancies. The ICON-ART predicted dust layer heights are 900 $\pm$ 693 m higher than those retrieved from lidar measurements between 13:00 on $19^{th}$ June and 02:00 on June $20^{th}$ 2021. The time series of particulate mass concentrations ($PM_{2.5}$ and $PM_{10}$) from Fidas measurements and dust mass concentration from the ICON-ART simulation, shown in Figure 5f, which have a slope of 0.56$\pm$ 0.106 and a Pearson correlation coefficient of 0.383. This remained discrepancy may be caused by the model sample location is different from measurement location with distance of 40 km. The vertical profiles of the backscatter coefficients from lidar retrievals and ICON-ART predictions for two selected periods indicated as C1 and C2 in Figure 5 are shown on the right side of Figure 5. For case C1, the backscatter coefficients predicted by ICON-ART for non-sherical particles is systematically lower than those retrieved from lidar measurements by a factor of 3.91 $\pm$ 1.66 between 2.6 - 4.4 km. There are two possible reasons for this underestimation of the backscatter coefficients. One is that ICON-ART underestimated the dust loading in this case and the a second possible explanation is that the Saharan dust particles interacted with cloud droplets within the layer. ERA5 temperature data indicate that temperatures were above 0 °C at the corresponding altitude, suggesting that liquid cloud droplets were more likely to form. The presence of cloud droplets can increase particle size and enhance the observed lidar backscatter, contributing to the elevated signal within the dust layer. For period C2, the backscatter coefficients predicted by ICON-ART were lower by a factor of 7.48 $\pm$ 1.9 below 3.2 km. The first reason for this difference of the backscatter coefficients is because of the additional presence of non-dust particles which are not included in this specific model calculation. So we separated the backscatter coefficients into the dust part and non-dust part as was done also for Saharan dust case 2, which shows that the presence of non-dust particles cannot explain the complete difference as the pure dust backscatter coefficients are still higher than those calculated by ICON-ART. The second possible reason for this remaining difference is that ICON-ART may underestimate the dust loading in the lower layer in this case. Although the ICON-ART results doesn't seem to agree with lidar measurements for this lower altitude, some consistency between model

simulations and lidar measurement can also be seen for the dust layer above. The dust layer between 3.2 - 6.0 km for period C2 is also shown on the right side of Figure 5 with a good agreement between model simulation and lidar measurement.

The discrepancy between the observed and simulated surface dust concentrations during Case 3 should therefore not be attributed solely to wet removal. Because this case was affected by clouds and precipitation, the comparison is sensitive to spatial displacement errors in the simulated cloud and precipitation fields, especially given the approximately 40 km distance between the model sampling location and the measurement site. In addition, the vertical overlap between dust, clouds, and precipitation may influence the simulated removal efficiency. However, the present observations do not allow a quantitative attribution of the model–observation difference to wet scavenging alone. This case highlights the importance of cloud-related processes for interpreting lidar observations and evaluating dust transport simulations.

#### 3.1.3 Extreme Saharan dust outbreak (Case 4)

The Saharan dust case 4 was observed at the KIT campus north from $16^{th}$ March 2022 to $21^{th}$ March 2022. This SAL was the most dense dust outbreak among all 4 cases with an AOD reaching values of $1.8 \pm 0.07$ at a wavelength of 550 nm in Karlsruhe (Kanngießer and Fiedler, 2026). Figure S5 shows the horizontal distribution of daily averaged aerosol optical depth (AOD) from MODIS satellite observations at a spatial resolution of $0.4° \times 0.4°$, for the period of March 16–21, 2021. During this time, Saharan dust originating in North Africa was transported toward Karlsruhe, Germany. The MODIS retrieval clearly depicts the presence of atmospheric SAL, exhibiting notably consistent spatial patterns. In particular, high AOD values over North Africa and the Middle East correspond well with established dust source regions. Figure 6 shows the time series of RCS for the polarized channel, cross-polarized channel, and LVDR from KASCAL measurements. The backscatter coefficients and particle depolarizations are not shown in this figure since their retrieval was impeded due to the presence of clouds from time to time. Figure 6 also shows the time series of ICON-ART predicted backscatter coefficients, particle number distributions, particulate matter concentrations, and ground level meteorological parameters (e.g. wind, precipitation, WS700). As can be seen from this figure, the Saharan dust layer arrived in Karlsruhe at 12:00 on $16^{th}$ March 2022 at an altitude between 2.0-3.5 km. Cloud cover was recorded after 00:00 on $17^{th}$, March 2022 with cloud base around 2.0 km. From 12:00 of $17^{th}$ March to 12:00 of $18^{th}$ March 2022, the presence of low level clouds and intermittent drizzle prevented the observation of the SAL by KASCAL. On midday of $18^{th}$ March 2022, another SAL arrived in Karlsruhe at an altitude of 2.0 - 3.0 km and subsequently sunk to lower altitudes. This latter SAL was less intensive than that observed on $16^{th}$ March 2022 as can be seen from the lower LVDR shown in panel (b) of this figure. The large particles observed at the surface by the Fidas 200 were not reproduced by the ICON-ART model, as shown in Figure 6f. In addition, two special periods (C1 and C2) are highlighted in this figure. These periods were used to further investigate dust properties measured by lidar and predicted by the ICON-ART model for different dust mass loadings. The evolution of the SAL over Karlsruhe for dust case 4 predicted by the ICON-ART model is shown in panel (d) of Figure 6. This plot shows that two SALs arrived at Karlsruhe during these six days. The first SAL arrived at Karlsruhe at 00:00 on $16^{th}$ March 2022 with an initial dust layer height between 2.0 - 4.0 km and lasted nearly 3 days. This SAL was relatively dense until 00:00 on $18^{th}$ March 2022 and was washed out by precipitation on 00:00 on $18^{th}$ March 2022. Another less dense SAL arrived at Karlsruhe at 06:00 on $21^{th}$ March 2022 at an altitude of 2.0-3.0 km. The dust layer heights

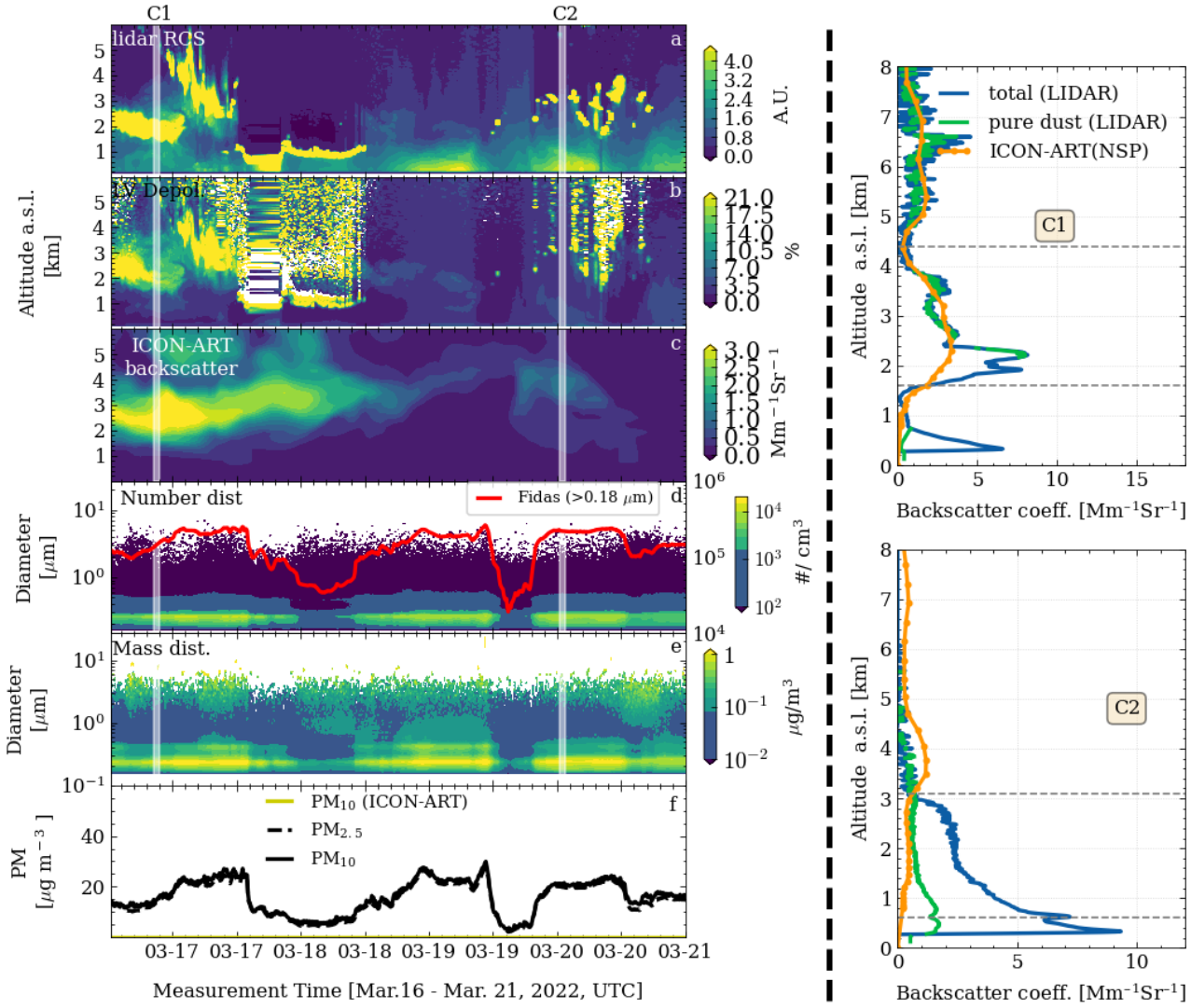



**Figure 6.** Time series of range corrected lidar signal for cross-polarized channel (a), and Linear Volume Depolarization Ratio (LVDR) (b) from KASCAL measurements, backscatter coefficients predicted by ICON-ART (c), particle number concentration (d), particle mass size distribution from Fidas 200 (e), and particulate matter concentrations $PM_{2.5}$ & $PM_{10}$ from the Fidas 200 and the lowest model level (150 m) of the ICON-ART simulation (f) from $16^{th}$ to $21^{th}$ March 2022 for case 4. The profiles of backscatter coefficients measured by the two lidars and predicted by ICON-ART model for C1 case (Averaged profiles from 20:30 to 21:30 for lidar measurement and profile at 21:00 for ICON-ART prediction on $16^{th}$ March 2022) and for C2 case (Averaged profiles from 00:30 to 01:30 for lidar measurement and profile at 01:00 for ICON-ART prediction on 20 $^{th}$ March 2022) are shown on the right side of this figure. C1 and C2 represent time periods used for a more detailed data analysis as shown in the right side of this figure.

and their peak heights for both lidar measurement and ICON-ART prediction for this Saharan dust case are shown in Figure 8d. The dust layer heights from ICON-ART prediction and lidar measurement show good agreement with each other. The vertical profiles of the backscatter coefficient from lidar retrieval and ICON-ART prediction for two selected periods indicated as C1 and C2 in Figure 6 are shown on the right side of Figure 6. For case C1, the vertical profile of backscatter coefficients predicted by ICON-ART agrees well with those retrieved from lidar measurements except for peak of backscatter coefficients at altitudes between 1.6 km and 2.4 km. One possible reason for this phenomenon is that the ICON-ART model cannot resolve this small scale vertical aerosol distributions. For case C2, the backscatter coefficients predicted by ICON-ART are significantly lower than those observed below 3.2 km. One possible reason for this difference is that ICON-ART overestimates the washout effect by precipitation in this case.

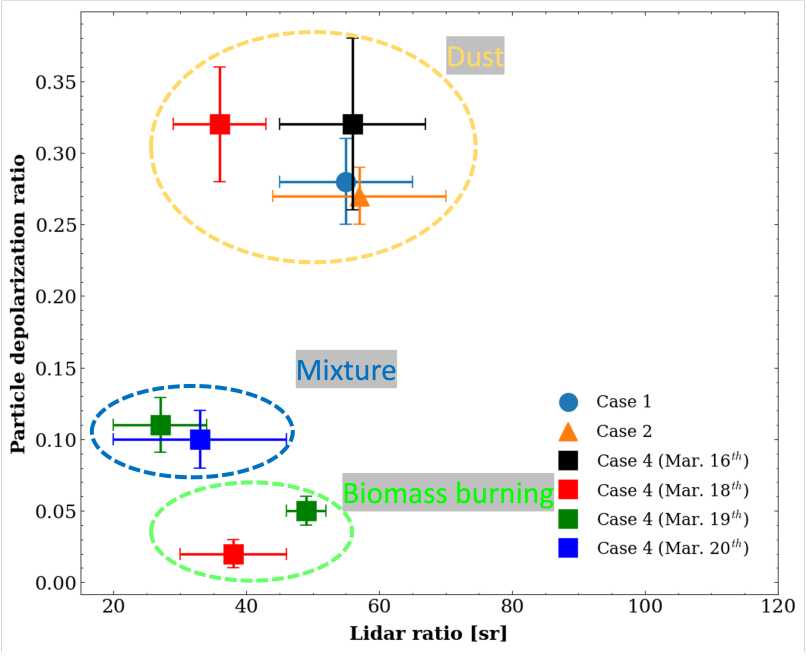



**Figure 7.** Linear Particle Depolarization Ratio (LPDR) versus lidar ratio retrieved from KASCAL for aerosol layers observed on different days across three Saharan dust cases. The lidar ratio for Case 3 is not available due to the absence of reliable lidar measurements during cloud-free nighttime periods.

Figure 7 presents the Linear Particle Depolarization Ratio (LPDR) versus lidar ratio retrieved from KASCAL for aerosol layers observed on different days for Saharan dust cases 1,2, and 4. The lidar ratio for Case 3 is not included due to the lack of reliable lidar data during cloud-free nighttime periods. For Cases 1 and 2, depolarization ratios of $0.28 \pm 0.03$ and $0.27 \pm 0.02$, and lidar ratios of $55 \pm 10$ sr and $57 \pm 13$ sr, respectively, were retrieved—values that are consistent with previous studies (Freudenthaler et al., 2009; Schuster et al., 2012; Cao et al., 2014). Case 4 reveals the presence of Saharan dust, continental

aerosol layers with low depolarization characteristics, and mixtures of these aerosol types. The backward-trajectory analysis indicates that the low-depolarization aerosol layers were transported within the lower troposphere over continental Europe, suggesting contributions from regional and local aerosol sources in addition to long-range transported Saharan dust. On $16^{th}$ March 2022, a dense dust layer was observed, characterized by a high depolarization ratio ($0.32 \pm 0.06$) and a lidar ratio of $56 \pm 11$ sr. On $18^{th}$ March, two distinct layers were identified: an upper dust layer (LPDR: $0.32 \pm 0.04$, lidar ratio: $36 \pm 7$ sr) and a lower low-depolarization aerosol layer (continental aerosol) (LPDR: $0.02 \pm 0.003$, lidar ratio: $38 \pm 8$ sr). On March 19, a mixed layer of Saharan dust and continental aerosols (LPDR: $0.11 \pm 0.019$, lidar ratio: $27 \pm 7$ sr) was observed below a continental aerosol layer (LPDR: $0.05 \pm 0.004$, lidar ratio: $49 \pm 3$ sr). By $20^{th}$ March, the layers had mixed more uniformly, with LPDR and lidar ratio values of $0.1 \pm 0.02$ and $33 \pm 13$ sr, respectively.The temporal evolution of LPDR and lidar ratio indicates a progressive transition from a dust-dominated aerosol column to a more complex aerosol mixture. While the optical properties of the low-depolarization layers are consistent with aerosol types commonly associated with anthropogenic pollution and aged biomass-burning particles, the trajectory analysis suggests a substantial contribution from regional and local aerosol sources. The gradual decrease in LPDR and the emergence of intermediate optical properties are consistent with increasing mixing between Saharan dust and regional aerosols during transport. This mixing results in intermediate depolarization values and variable lidar ratios, depending on the relative abundance of dust and low-depolarization layers in the column. These findings underscore the complexity of aerosol interactions and their evolving optical properties during long-range transport events involving multiple sources. The observed aerosol layering illustrates that realistic representation of aerosol mixing is essential for accurately simulating optical properties during long-range transport.

### 3.2 Statistical comparison of optical and microphysical properties

Table 2 summarizes the key optical parameters of Saharan dust retrieved from lidar and sun-photometer observations for all four investigated cases. As noted earlier, the lidar ratio for Case 3 is not reported because no reliable lidar signals were available during cloud-free nighttime periods, and the single-scattering albedo (SSA) for this case is also excluded due to persistent cloud contamination. Overall, the retrieved optical properties exhibit values that are consistent with well-established characteristics of transported Saharan dust. In particular, the lidar ratios (LR), depolarization ratios, and SSA values fall within the range of previously reported measurements over North Africa and downwind regions (Freudenthaler et al., 2009; Schuster et al., 2012; Cao et al., 2014; GROß et al., 2011; Tesche et al., 2009a). This agreement suggests that our retrieval procedure accurately captures the microphysical and radiative signatures of mineral dust. Taken together, the close agreement with established climatological values and the physically consistent variability across cases provide confidence in the robustness of our observational dataset and support its relevance for evaluating dust representations in radiative transfer models and numerical simulations.

Figure 8 shows the time series of dust base height, dust top height, and dust peak height for both lidar measurements and ICON-ART simulations. This figure shows that the dust arrival times predicted by the ICON-ART model agrees well with lidar measurements ($\pm$ 20 minutes) and in general for dust layer height ($\pm$ 50 m) in all 4 cases. However, ICON-ART also tends to overesimate the dust layer height (e.g. the first half of case 2 as shown in Figure 8b). The remaining discrepancies between

**Table 2.** Overview of optical parameters of Saharan dust determined from lidar data, sun photometer measurements, and ICON-ART simulations for all four Saharan dust cases.

| Parameter | $\lambda$ [nm] | Case 1 | Case 2 | Case 3 | Case 4 | Average | Reference |
|---|---|---|---|---|---|---|---|
| BSC. ($Mm^{-1}sr^{-1}$) | 355 | $0.95 \pm 0.23$ | $0.91 \pm 0.43$ | $1.52 \pm 0.31$ | $3.17 \pm 2.48$ | $1.64 \pm 0.70$ | this work (lidar) |
| BSC. ($Mm^{-1}sr^{-1}$) | 355 | $0.71 \pm 0.37$ | $1.15 \pm 0.41$ | $0.73 \pm 0.30$ | $0.77 \pm 0.73$ | $0.84 \pm 0.47$ | this work (ICON-ART) |
| LPDR | 355 | $0.28 \pm 0.03$ | $0.27 \pm 0.02$ | $0.31 \pm 0.04$ | $0.30 \pm 0.03$ | $0.29 \pm 0.03$ | $0.252 \pm 0.03$ (Haarig et al. 2017) |
| LR (sr) | 355 | $46 \pm 10$ | $57 \pm 13$ | | $55 \pm 10$ | $53 \pm 11$ | $48 \pm 8$ (Haarig et al. 2022) |
| AOD | 340 | $0.21 \pm 0.12$ | $0.33 \pm 0.12$ | $0.52 \pm 0.14$ | $0.80 \pm 0.42$ | $0.47 \pm 0.20$ | this work (sun photometer) |
| AOD | 500 | $0.25 \pm 0.11$ | $0.39 \pm 0.12$ | $0.57 \pm 0.12$ | $0.91 \pm 0.42$ | $0.53 \pm 0.19$ | this work (sun photometer) |
| AOD | 550 | $0.17 \pm 0.09$ | $0.36 \pm 0.22$ | $0.24 \pm 0.10$ | $0.18 \pm 0.06$ | $0.24 \pm 0.12$ | this work (ICON-ART) |
| AOD | 1020 | $0.30 \pm 0.11$ | $0.41 \pm 0.14$ | $0.69 \pm 0.12$ | $1.01 \pm 0.43$ | $0.60 \pm 0.20$ | this work (sun photometer) |
| SSA | 439 | $0.92 \pm 0.03$ | $0.90 \pm 0.27$ | | $0.93 \pm 0.01$ | $0.91 \pm 0.10$ | 0.91 (Müller et al., 2011) |
| SSA | 870 | $0.93 \pm 0.04$ | $0.95 \pm 0.23$ | | $0.95 \pm 0.01$ | $0.94 \pm 0.09$ | 0.86 - 0.98 (Cachorro et.al., 2018) |

BSC: backscatter coefficient; Exc: extinction coefficient; LR: lidar ratio; LPDR: linear particle depolariization ratio.
AOD: Aerosol optical depth, SSA: single scatter albedo

observations and ICON-ART predictions may be related to the following reasons: 1) Excessive vertical transport of dust in ICON-ART: During long-range transport, ICON-ART may transport dust particles to higher altitudes than observed, resulting in an overly elevated simulated dust layer and contributing to discrepancies in the modeled vertical dust distribution. 2) Low lidar sensitivity to elevated dust layers: At higher altitudes, the lidar measurements are characterized by a relatively low signal-to-noise ratio because of the weaker aerosol backscatter signal. This increases the uncertainty in detecting and quantifying tenuous dust layers aloft and may partly explain the differences between the modeled and observed dust vertical distributions.

Figure 9 shows the correlation of dust base heights, dust peak heights, and dust top heights from lidar measurements and

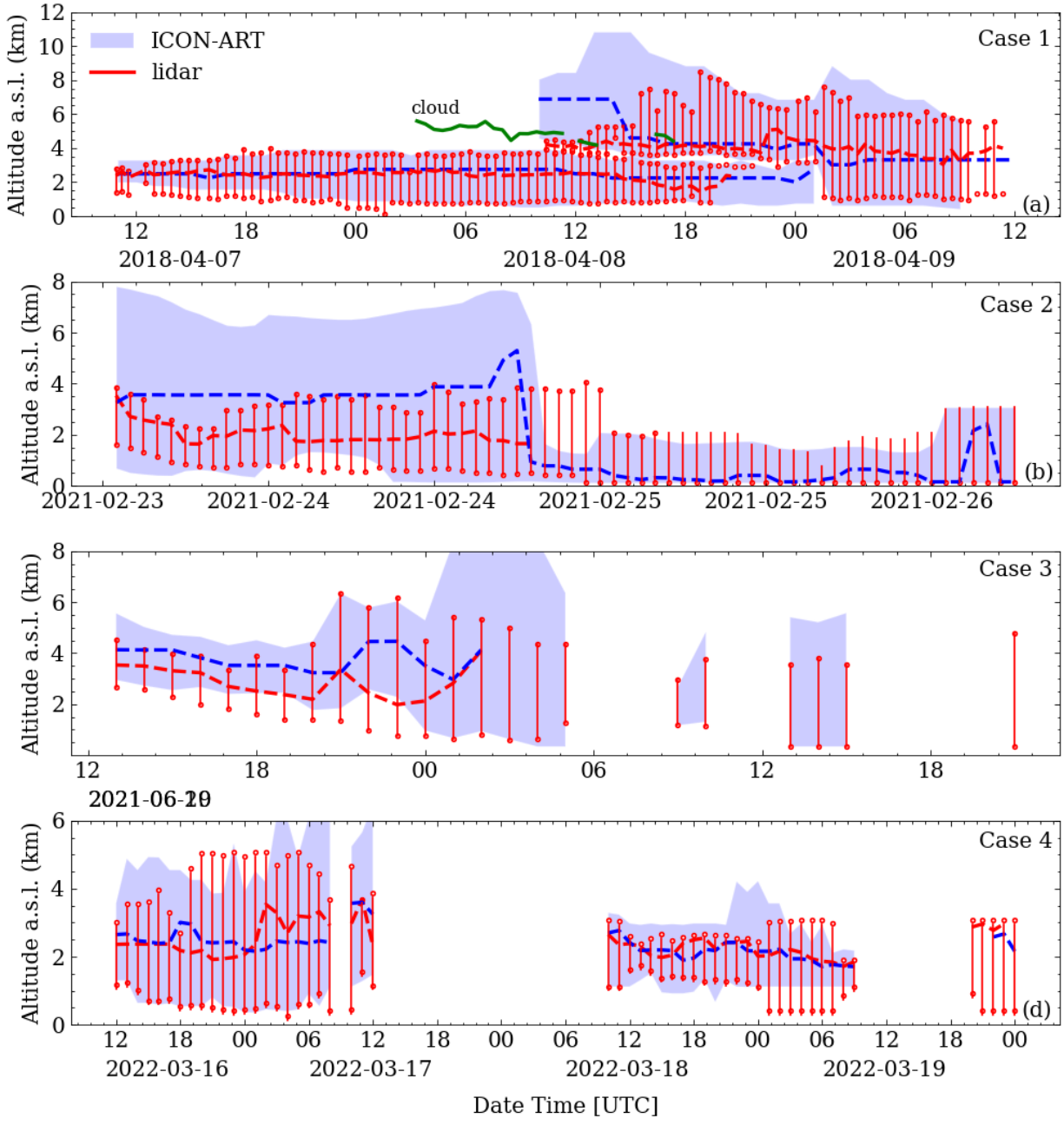



**Figure 8.** Time series of Saharan dust layer heights (vertical extend) and their peak heights (heights of maximum backscatter coefficients, indicated as red (lidar) and blue (ICON-ART) solid line) from both lidar measurements (red bars) and ICON-ART predictions (light blue area) for cases 1 - 4.

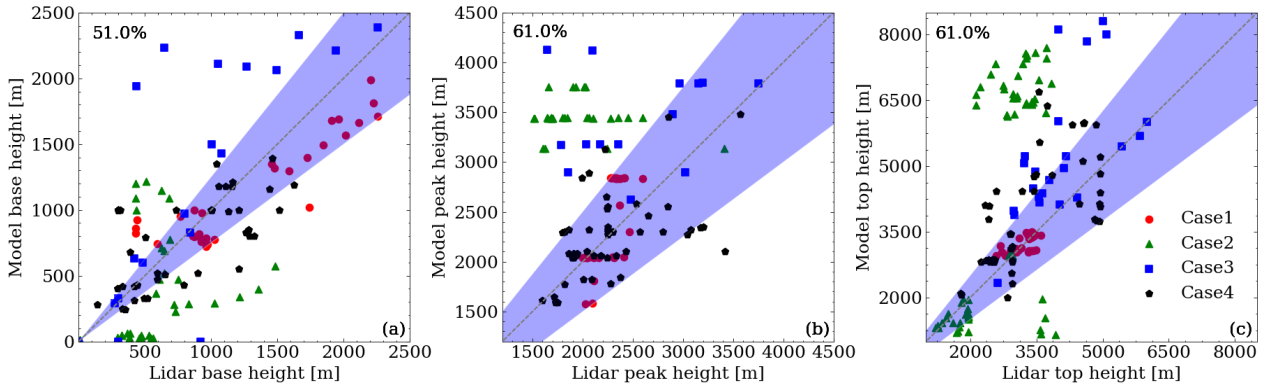



**Figure 9.** Correlation of dust base heights (a), dust peak heights (b), and dust top heights (c) from lidar measurements and ICON-ART simulations for all 4 Saharan dust cases.The blue-shaded area indicates slopes between 0.75 and 1.25 and the number shown in the left upper corner is the percentage of data points within this blue-shaded area.

ICON-ART predictions for the four Saharan dust cases. These plots show that there are 51%, 61%, and 61% of all data points within this blue-shaded area for dust base heights, dust peak heights, and dust top heights, respectively. To be clear, good agreement in dust layer heights can be seen for case 1, case 3, and case 4 but not for case 2 as discussed before. In general, the ICON-ART model predicts dust arrival times and dust layer heights very well if considering the spatial resolution of the ICON-ART model (26.0 km horizontally).

### 3.3 Model performance under different resolutions and initialization

Figure 10 compares the observed Saharan dust evolution over KIT-CN with simulations from the two experiments, namely the continuous 5-day forecast experiment (EXP-5d) and the daily re-initialized forecast experiment (RI-EXP-1d) for global (26 km with 13 km nest) and LAM runs (2 km, with 1 km nest). Here, only the results from the 26 km and 1 km simulations are shown, while the results from the 13 km and 2 km simulations are provided in Figure S6. It has to be noted that the effective resolution of resolved processes by the model is still around 5-6 horizontal resolution. At the synoptic scale, both experiments successfully reproduce the timing of the Saharan dust outbreak and the overall transport pathway from North Africa towards Central Europe. However, substantial differences are evident in the vertical structure and intensity of the simulated dust layers. Compared to EXP-5d, the RI-EXP-1d simulations show a more realistic representation of the observed dust layer heights, backscatter gradients, and near-surface PM10 concentrations. This improvement is likely related to the reduction of accumulated meteorological forecast errors through daily re-initialization. It has to be noted that the re-initialization for global run also introduces new states for the dust besides the meteorological states. But the LAM runs are only affected by the new boundary conditions. So, discontinuities in the dust fields for RI-EXP-1d is visible only for global runs. Since the meteorological analyses are continuously refreshed, the large-scale circulation, frontal structures, and associated vertical motions remain closer to

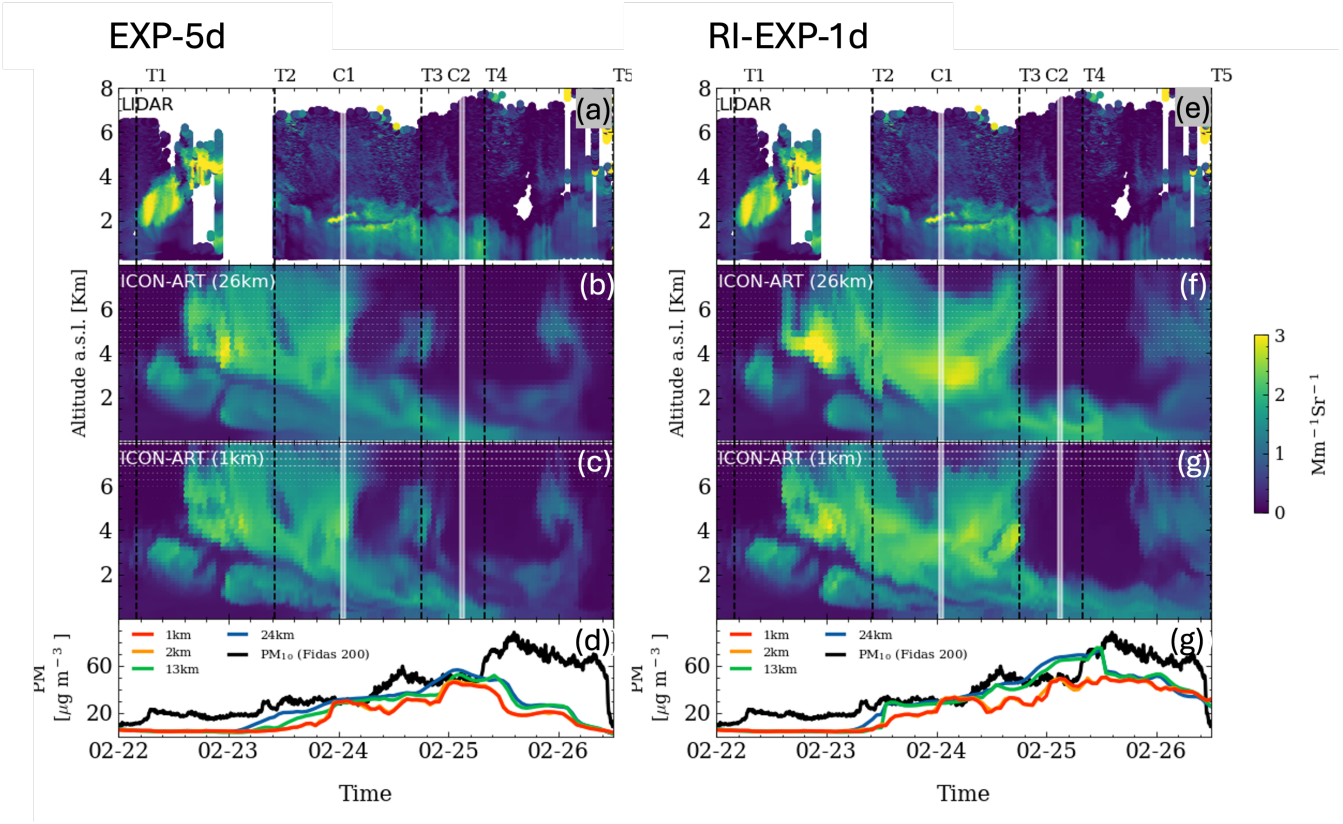



**Figure 10.** Time–height cross section of lidar backscatter coefficient(a). Corresponding ICON-ART backscatter coefficient simulated at horizontal grid spacings of 26 km, and 1 km, respectively(b–c). Time series of surface PM concentration measured by Fidas 200 (black) and simulated by ICON-ART (f) from $22^{nd}$ to $26^{th}$ February 2021. Panels (f–g) are the same as panels (b–d), but for the RI-EXP-1d experiment.

the observed atmospheric state throughout the event.

Despite the improved meteorological forcing, differences between the simulations and observations remain. This is expected because the re-initialization procedure only constrains meteorological variables, while no corresponding assimilation is available for mineral dust tracers. Consequently, uncertainties associated with dust emission, deposition, and aerosol transport processes continue to evolve freely within the model. These uncertainties can accumulate during transport from the Saharan source regions and may contribute to discrepancies in both dust concentration and vertical distribution, even when the meteorological conditions are well represented.

The general structure of time-height cross-section plot of the backscatter remains similar across resolution. The impact of model resolution becomes visible when comparing the surface $PM_{10}$ concentraton and the vertical profiles of the simulated dust structures (cf. Figure 11) with close resemblance for 26/13 and 2/1km respectively. The differences can be observed both in the boundary layer and the upper layers. The differences are more pronounced in the RI-EXP-1d experiment with high-

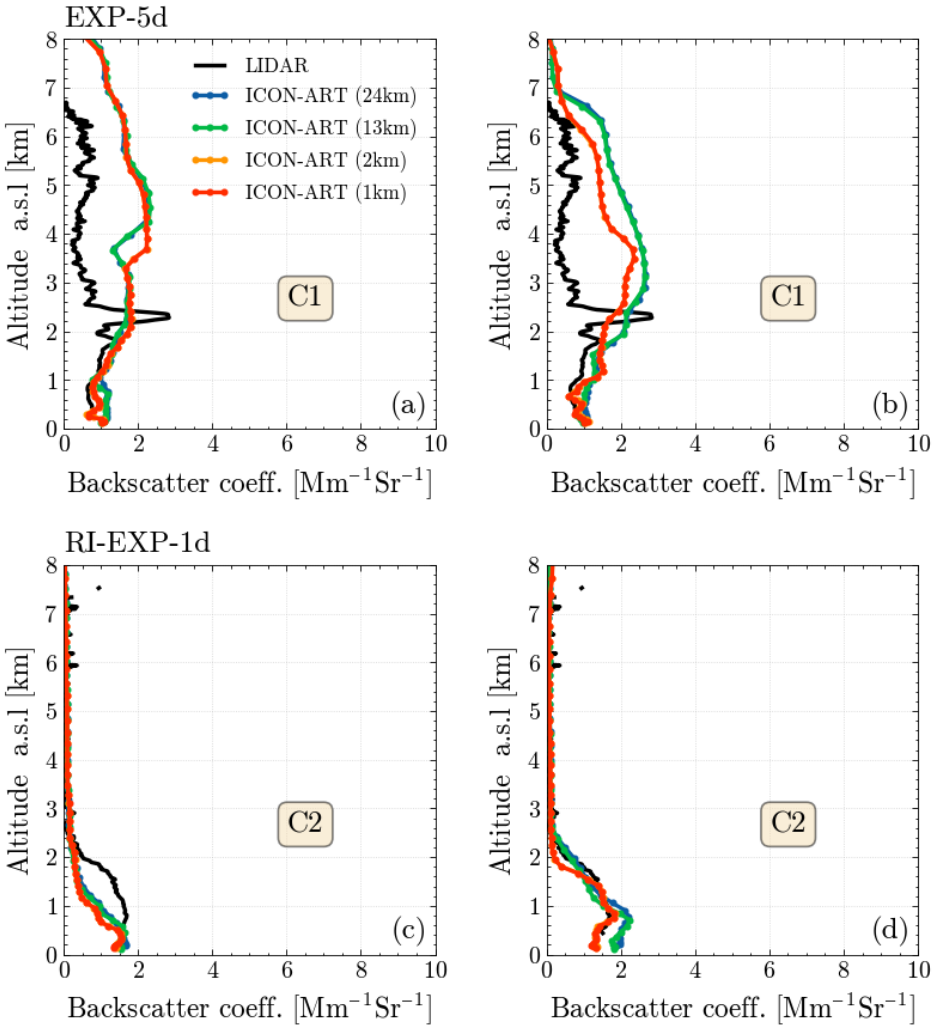



**Figure 11.** Profiles of pure dust backscatter coefficients measured by the lidar and predicted by ICON-ART model for case C1 (g: averaged profiles from 00:30 to 1:30 for lidar measurement and profile at 01:00 for ICON-ART prediction on $24^{th}$ February 2021) and for case C2 (h; averaged profiles from 02:30 to 03:30 for lidar measurement and profile at 03:00 for ICON-ART prediction on $25^{th}$ February 2021).

475 resolution runs in better agreement with the observed vertical dust profiles in the boundary layer. It also tends to decrease the backscatter in the upper layers. Compared to the EXP-5d runs, here the boundary condition is updated every day for the high resolution limited area runs. This shows that accurate lateral boundary conditions coupled with high resolution runs can improve the simulated dust transport.

Overall, the results indicate that both forecast strategy and model resolution contribute to simulation quality. Daily re-initialization
480 reduces the influence of accumulated meteorological forecast errors, while kilometer-scale resolutions improve the representation of mesoscale and boundary-layer processes that govern the detailed vertical structure of transported Saharan dust.

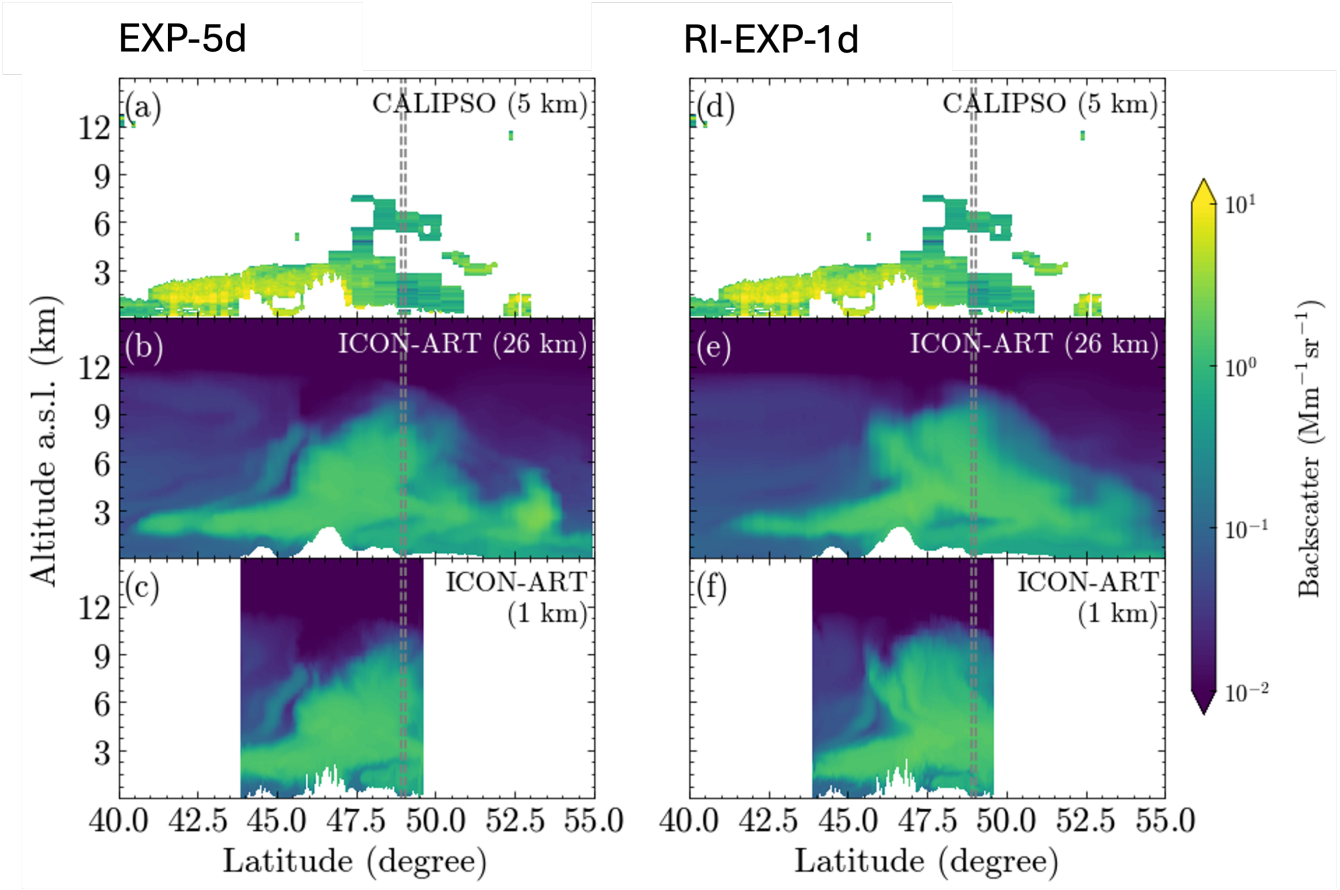



**Figure 12.** Latitude height of backscatter coefficient at 532 nm from CALIPSO retrieval (a) and ICON-ART simulation for horizontal grid spacings of 26 km and 1 km, respectively(b–c). Panels (e-f) are the same as panels (b–c), but for the RI-EXP-1d experiment. The data was sampled at 13:00 UTC on 23 February 2021.

The comparison between the ground-based lidar observations and the ICON-ART simulations at different horizontal resolutions for period C1 indicates that the model reasonably reproduces the observed dust layer below approximately 2.6 km. However, all ICON-ART simulations systematically overestimate the backscatter coefficient between approximately 2.6 and 8 km. To further investigate this discrepancy, we additionally compared the ground-based lidar observations with CALIPSO retrievals, as shown in Figure 12. The closest distance between the CALIPSO ground track and the KIT-CN observation site was approximately 20 km. Figure 12 shows the latitude–height cross section of the aerosol backscatter coefficient from the CALIPSO retrieval at 532 nm and the corresponding ICON-ART simulations at horizontal grid spacings of 26 km and 1 km for both EXP-5d (b-c) and RI-EXP-1d (e-f) experiments. The results from the 13 km and 2 km simulations are provided in Figure S7. This figure show that ICON-ART model shows agreement with CALIPSO retrievals in term of dust height and dust structure. In addition, kilometer-scale simulations provided a more realistic representation of dust-layer stratification and fine-

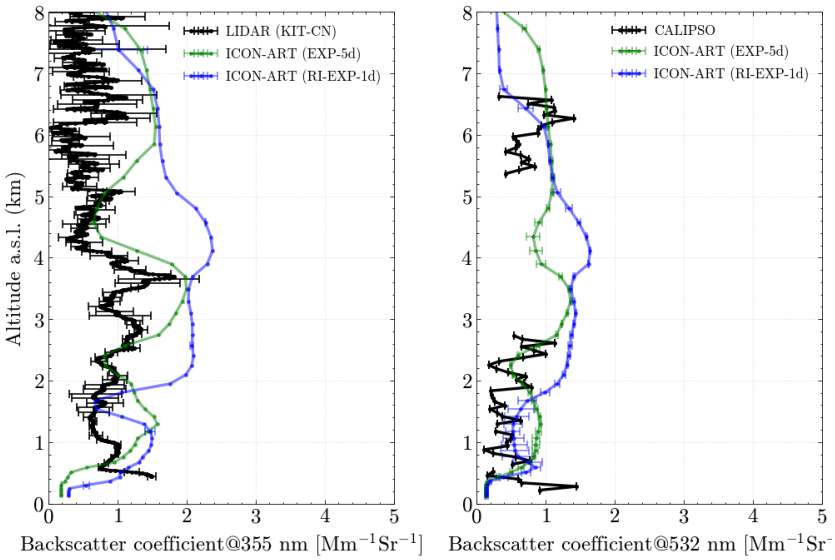



**Figure 13.** Vertical profiles of the aerosol backscatter coefficients from ground-based lidar observations and ICON-ART simulation (1 km) for both EXP-5d and RI-EXP-1d experiments at 355 nm (left) as well as vertical profiles of the aerosol backscatter coefficient from CALIPSO retrievals and the ICON-ART simulation (1 km) for both EXP-5d and RI-EXP-1d experiments at 532 nm. The data was sampled at 13:00 UTC on 23 February 2021.

scale vertical structures. The comparison of EXP-5d experiments with RI-EXP-1d experiments shown in Figure S8 illustrates the impact of initialization conditions on simulation result. In contrast to EXP-5d (left), where no clear resolution dependence is observed, RI-EXP-1d (right) exhibits a pronounced resolution dependence, especially between 7 and 8 km altitude. In this altitude range, the kilometre-resolution RI-EXP-1d simulations show reduced backscatter coefficients compared with the coarser-resolution simulations, leading to better agreement with the CALIPSO retrievals. This suggests that, for RI-EXP-1d, increasing the horizontal resolution improves the representation of the upper part of the dust layer, while this improvement is not evident in the EXP-5d simulations.

Figure 13 presents vertical profiles of the aerosol backscatter coefficient from ground-based lidar observations and the 1-km ICON-ART simulations for the EXP-5d and RI-EXP-1d experiments at 355 nm (left), together with the corresponding profiles from CALIPSO retrievals and the 1-km ICON-ART simulations at 532 nm (right). The comparison reveals a clear wavelength-dependent behavior in the model performance. At 355 nm, ICON-ART generally overestimates the aerosol backscatter coefficient relative to the KASCAL retrievals, particularly between 5.2 and 6.6 km, whereas at 532 nm the simulated profiles show substantially better agreement with the CALIPSO observations. This suggests that the simulated aerosol optical properties exhibit a stronger spectral dependence than indicated by the lidar observations. The contrasting model performance at 355 and 532 nm points to a potential bias in the particle size distribution represented in ICON-ART. In particular, an excessive contribution from relatively small and intermediate-sized particles would enhance backscattering more strongly at shorter wavelengths, leading to a larger simulated backscatter coefficient at 355 nm relative to 532 nm. This interpretation is consistent with the

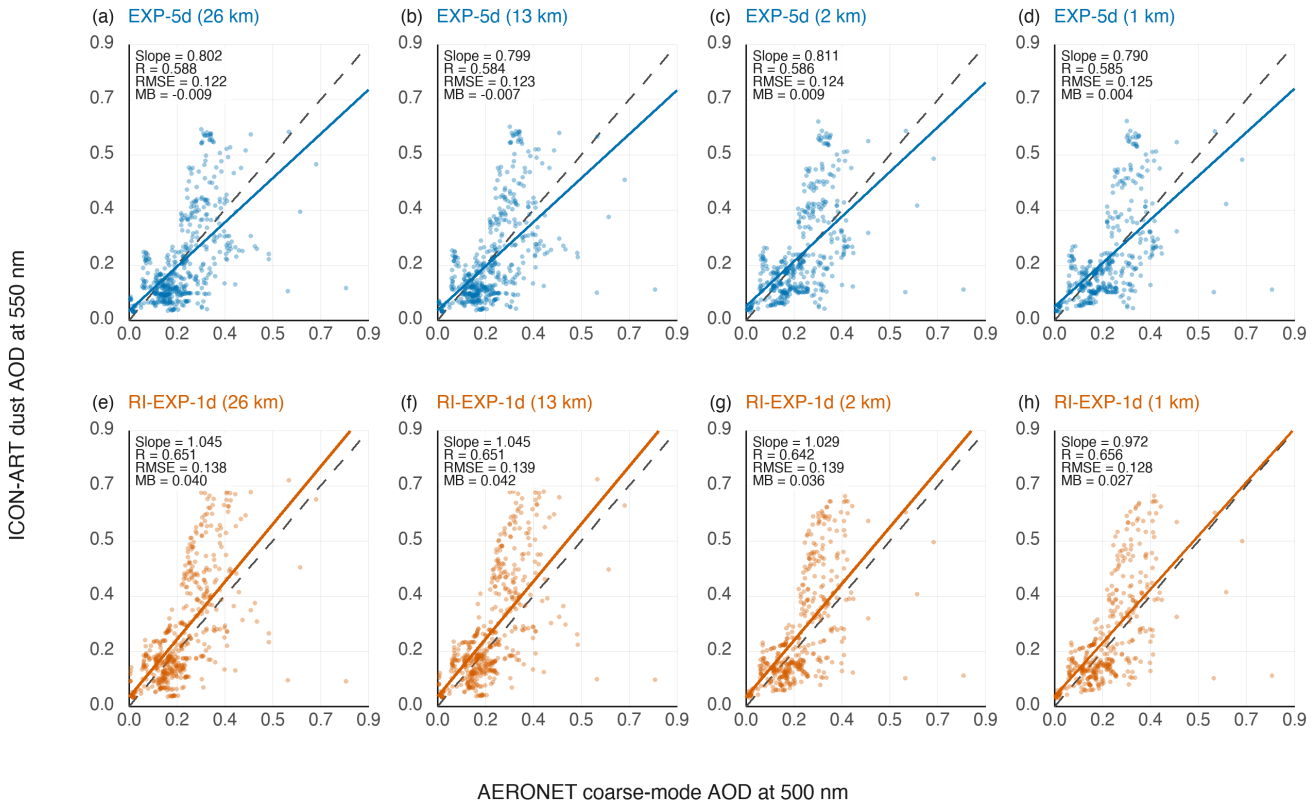



**Figure 14.** Comparison of AERONET coarse-mode AOD and ICON-ART-simulated dust AOD for the EXP-5d (a–d) and RI-EXP-1d (e–h) simulations at horizontal grid spacings of 26, 13, 2, and 1 km. The analysis is restricted to the innermost model domain, which contains 17 AERONET sites. Solid lines represent the least-squares linear regressions, and dashed lines indicate the 1:1 relationship. The reported statistics are the regression slope, Pearson correlation coefficient (r), root-mean-square error (RMSE), and mean bias (MB; model minus observation).

comparison against the Fidas 200 measurements (cf. Figure S9), which shows that ICON-ART underestimates the abundance of coarse particles while overestimating particles in the intermediate size range. Because coarse particles generally exhibit a weaker wavelength dependence of their optical properties than smaller particles, this shift in the simulated size distribution toward smaller sizes can result in an excessively strong spectral dependence of the aerosol backscatter coefficient.

Figure 14 compares the ICON-ART dust AOD with the AERONET coarse-mode AOD for the EXP-5d and RI-EXP-1d simulations at four horizontal grid spacings. ICON-ART captures the variability in AERONET coarse-mode AOD reasonably well across all four horizontal grid spacings, although the agreement depends more strongly on the experimental configuration than on grid resolution. For a given configuration, the correlation coefficients and other statistical metrics remain largely insensitive to changes in horizontal grid spacing from 26 to 1 km. The standard EXP-5d simulations yield correlations of r=0.584–0.588

and regression slopes of 0.790–0.811. The slopes of approximately 0.8 indicate that the model increasingly underestimates AOD as the observed AOD increases, despite the small mean biases (-0.009 to 0.009). RI-EXP-1d increases the correlations to r=0.642–0.656 and brings the regression slopes closer to unity (0.972–1.045), indicating an improved representation of the observed AOD magnitude and variability. However, this improvement is accompanied by positive mean biases of 0.027–0.042 and does not lead to a systematic reduction in RMSE. Among the RI-EXP-1d simulations, the 1 km simulation shows the closest agreement, with r=0.656, a slope of 0.972, an RMSE of 0.128, and a mean bias of 0.027. These optical comparisons should, however, be interpreted in light of uncertainties in the particle size distribution (PSD) assumed in ICON-ART, as the PSD directly affects the conversion of simulated aerosol mass into optical properties. This issue is particularly relevant to the coarse mode: ICON-ART substantially underestimates both $PM_{10}$ and coarse-particle mass and underrepresents the pronounced contribution of particles larger than approximately 5$\mu$m evident in the observations, as shown in Figure S9 and reported in previous studies (Hoshyaripour et al., 2019). Consequently, part of the remaining AOD discrepancy may arise from uncertainties in the assumed PSD and the associated optical properties, in addition to the underestimated coarse-aerosol burden. The persistence of similar AOD statistics across resolutions therefore suggests that the dominant discrepancies are related to aerosol representation, including the coarse-particle size distribution and mass, and/or model–observation differences, rather than spatial resolution alone.

Figure 15 presents the time series of ground-level aerosol mass size distributions (dM/dlnD) measured by the Fidas 200 optical particle spectrometer and the corresponding dust mass size distributions simulated by ICON-ART at horizontal resolutions of 26 km, 13 km, 2 km, and 1 km. The model results from both the continuous 5-day forecast experiment (EXP-5d) and the daily re-initialized forecast experiment (RI-EXP-1d) are shown. Both the observations and simulations indicate that the dust particles reached the surface during the period from approximately 10:00 UTC on 23 February to 12:00 on $26^{th}$ February 2021. During this period, enhanced concentrations of coarse-mode particles were observed by the Fidas 200 instrument and reproduced by ICON-ART, confirming the downward transport of mineral dust into the boundary layer. The RI-EXP-1d experiment generally shows better agreement with the observations in terms of both the timing and duration of the surface dust event. In contrast, the EXP-5d simulations, particularly at 2 km and 1 km resolution, tend to underestimate the duration of the near-surface dust occurrence and simulate a shorter period during which the SAL remains in contact with the surface. This result suggests that errors accumulated in the meteorological fields during the continuous 5-day forecast can affect the representation of boundary-layer processes and vertical dust transport. Small deviations in the simulated wind field, boundary-layer depth, or vertical mixing can lead to substantial differences in the timing and persistence of dust reaching the surface. The differences among model resolutions further indicate that the surface concentration of transported dust is sensitive to mesoscale and local-scale dynamical processes. While the coarser simulations reproduce the overall temporal evolution of the dust event, the kilometer-scale simulations resolve finer-scale structures in the boundary layer and topographically induced circulations that influence the vertical redistribution of dust. However, these high-resolution simulations are also more sensitive to inaccuracies in the meteorological forcing. Consequently, the benefits of increased spatial resolution become most evident when combined with improved meteorological initialization, as demonstrated by the RI-EXP-1d experiment. Overall, the results suggest that an accurate representation of both meteorological conditions and mesoscale transport processes is essential for reproducing the

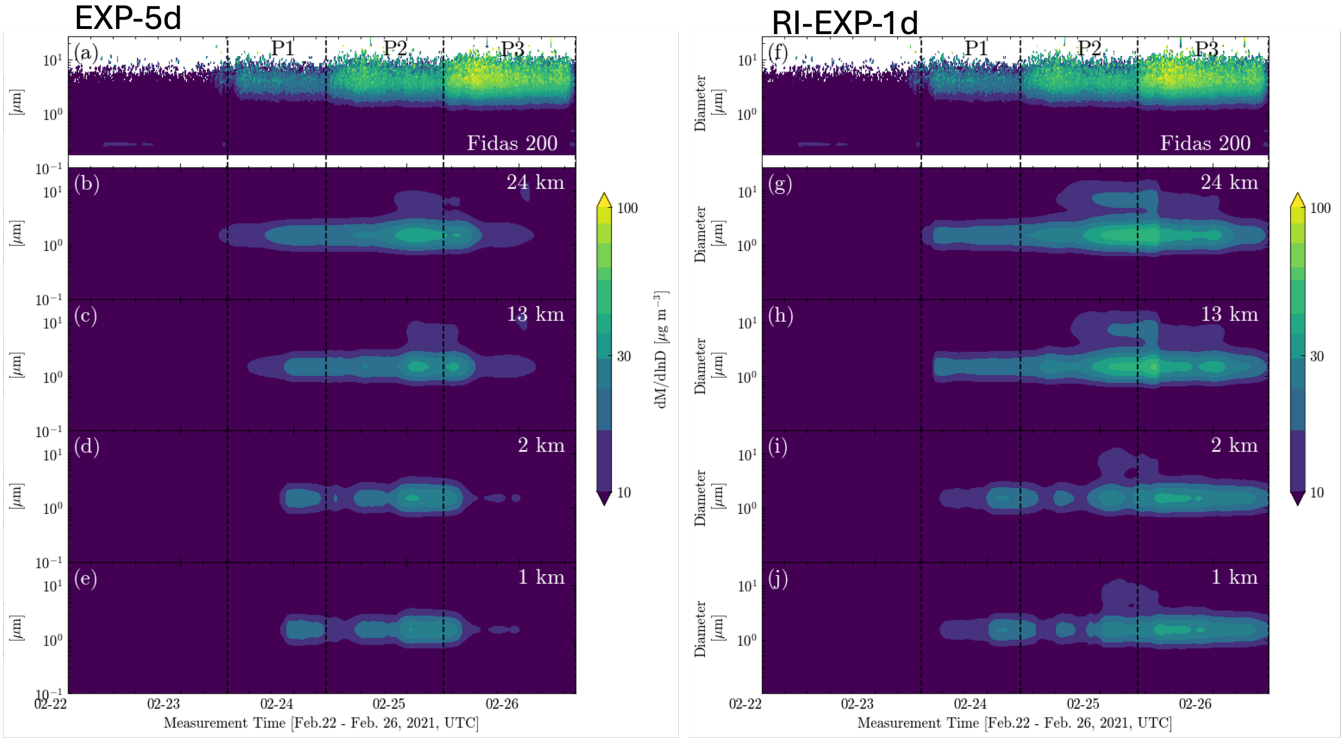



**Figure 15.** Time series of ground-level aerosol mass size distributions (dM/dlnD) measured by the Fidas 200 optical particle spectrometer (a) and simulated dust mass size distributions from ICON-ART at horizontal resolutions of 26 km, 13 km, 2 km, and 1 km (b-e). Results from EXP-5d experiment (b-e) and RI-EXP-1d experiment (g-j) are presented for the Saharan dust event of $21^{st}$–$25^{th}$ February 2021.

timing, duration, and size-dependent characteristics of surface Saharan dust concentrations.

The averaged aerosol/dust size distributions during the three periods (P1, P2, and P3 in Figure 15) are shown in Figure S9. Overall, the ICON-ART simulations reproduce the general shape and temporal evolution of the observed size distributions during the Saharan dust event. However, systematic biases are evident across all periods. The model tends to overestimate the mass concentration for particle diameters between approximately 0.5 and 2 $\mu$m, while underestimating the mass concentration for particles larger than 2 $\mu$m. A similar conclusion was reached by Ratcliffe et al. (2025), who showed that additional processes counteracting the rapid sedimentation of coarse dust particles are required for climate models to reproduce observations. This behaviour suggests that the simulated dust size distribution is shifted toward smaller particle sizes compared with the observations. The underrepresentation of coarse particles may be related to excessive removal of large dust particles during transport through gravitational settling and dry deposition, insufficient emission of coarse-mode dust at the source regions, or uncertainties in the prescribed dust size distribution. Consequently, the model retains too much mass in the accumulation mode while underestimating the contribution of coarse-mode particles at the observation site. The persistence of this bias in both the EXP-5d and RI-EXP-1d experiments indicates that the discrepancies in the size distributions are likely associated with un-

certainties in dust microphysical processes and size-dependent deposition rather than meteorological initialization. While the daily re-initialization improves the representation of the dust-layer structure and transport pathways, it has a relatively limited impact on the simulated surface size spectra. These results suggest that further improvements in the parameterization of dust emission, sedimentation, and deposition processes are required to accurately reproduce the observed particle size distributions during long-range Saharan dust transport events.

## 4 Discussion

The comparison of observations with ICON-ART simulations for four Saharan dust events and two sensitivity experiments provides insight into the main sources of model-observation discrepancies. Three main findings emerge. First, the large-scale transport pathway and plume arrival time are reproduced consistently across all model resolutions and meteorological initialization strategies, with a mean arrival-time difference of approximately 20 min even at 20 km horizontal resolution. Second, the aerosol loading and vertical distribution of dust are strongly influenced by both horizontal resolution and meteorological initialization, with the best agreement achieved only when both are improved simultaneously. Third, the particle size distribution and some systematic features of the optical properties remain largely unchanged across all experiments, suggesting that these persistent discrepancies originate from the aerosol representation rather than from the transport itself.

The improvement in the simulated vertical dust structure is one of the main findings of this study. Compared with the continuous 5-day forecast (EXP-5d), the daily re-initialized forecast (RI-EXP-1d) increases the correlation between simulated and observed near-surface $PM_{10}$ concentrations from $R = 0.65$–$0.69$ to $R = 0.86$–$0.88$ across all model resolutions, while reducing the RMSE by approximately one third. The RI-EXP-1d also increases the correlation between simulated and observed AOD from $R = 0.29$-$0.31$ to $R = 0.41$–$0.42$ (Table S1). These results show that daily re-initialized forecast provides better representation of both surface dust concentration and column-integrated aerosol concentration. This sensitivity to meteorological forcing agrees with previous studies showing that Saharan dust outbreaks contribute to short-range forecast uncertainty over Europe (Hermes et al., 2024) and that updated meteorological analyses improve aerosol forecast skill in operational forecasting systems (Benedetti et al., 2009). The improvement is not solely attributable to increased horizontal resolution. Similar improvements from EXP-5d to RI-EXP-1d are found at both coarse (26 and 13 km) and convection-permitting (2 and 1 km) resolutions, indicating that reducing accumulated meteorological forecast errors substantially improves the timing and duration of near-surface dust events. Higher resolution provides an additional benefit by resolving circulations and enhancing vertical exchange between the free troposphere and the boundary layer, resulting in sharper dust-layer boundaries and a reduced overestimation of elevated dust concentrations (Figure 10 and 12). These findings are consistent with previous studies demonstrating that convection-permitting simulations improve the representation of dust-related vertical transport processes associated with convective downdrafts and cold pools (Marsham et al., 2011; Heinold et al., 2013). However, higher resolution alone does not compensate for deficiencies in the meteorological forcing. In the EXP-5d simulations, the 1 and 2 km experiments underestimate the duration of the near-surface dust event more strongly than the coarser-resolution simulations because accumulated meteorological errors are more directly reflected in the better-resolved boundary-layer transport. These results demonstrate

that meteorological initialization and horizontal resolution provide complementary improvements, with the best performance obtained when both are combined.

At first glance, the backscatter-profile statistics appear inconsistent with the improvements obtained for near-surface $PM_{10}$. The normalized mean bias of the lidar-model comparison is smaller for EXP-5d (5.9–6.5 %) than for RI-EXP-1d (38–50 %), whereas RMSE and correlation remain similar in both experiments ($R \approx 0.37$–$0.41$) (Table S1). This behaviour is most likely explained by compensating errors rather than improved model performance. The comparison with CALIPSO observations (Figure 13 and S8) shows that all simulations, including the 1 km RI-EXP-1d experiment, systematically overestimate backscatter above approximately 2.6 km. A continuous forecast may therefore produce a smaller overall bias if underestimation at one altitude compensates for overestimation elsewhere, without improving the vertical profile itself. This interpretation is supported by the nearly unchanged RMSE between EXP-5d and RI-EXP-1d. Similar limitations of profile-integrated bias metrics have been reported previously, and profile-resolved statistics are generally recommended for evaluating vertically resolved aerosol simulations (Binietoglou et al., 2015). Consequently, the backscatter results do not contradict the improvements in vertical dust transport but instead indicate that improved meteorological forcing and resolution improve the vertical redistribution of dust without correcting the persistent overestimation of elevated aerosol layers.

The overestimation of elevated dust layers forms part of a broader pattern that is largely unaffected by either model resolution or meteorological initialization. ICON-ART overestimates the backscatter coefficient at 355 nm (KASCAL) but show agreement with the backscatter coefficient at 532 nm (CALIPSO). This wavelength-dependent behaviour is consistent with ICON-ART underestimating the abundance of coarse particles while overestimating intermediate-sized particles. This interpretation is independently supported by the particle mass size distributions measured by the Fidas 200 (Figure 15 and S8). ICON-ART consistently overestimates particles between approximately 0.5 and 2 $\mu$m while underestimating particles larger than 2 $\mu$m, and these biases remain nearly unchanged in both EXP-5d and RI-EXP-1d. Since meteorological re-initialization substantially improves the timing and duration of surface dust events without affecting the particle size distribution, the remaining discrepancy likely reflects limitations in the representation of the emitted size distribution and the size-dependent removal of coarse particles, potentially through sedimentation and dry deposition during long-range transport. This interpretation is consistent with previous studies. Ratcliffe et al. (2025) showed that additional processes are required to maintain coarse dust during atmospheric transport, while Adebiyi and Kok (2020) demonstrated from a global synthesis of in-situ observations that current models remove coarse dust too efficiently. The present study extends these findings to long-range Saharan dust transport over Europe using both remote sensing and in-situ observations.

Wet deposition represents another potential source of uncertainty, particularly during Case 3. Observations show that moderate precipitation efficiently removed dust from the boundary layer. However, the present analysis does not allow a robust assessment of the wet deposition parameterization because the model evaluation point is located approximately 40 km from the observation site and precipitation was spatially heterogeneous. Consequently, differences between simulated and observed dust concentrations may partly reflect spatial displacement of precipitation rather than deficiencies in the wet removal scheme itself. Wet deposition should therefore be regarded as an important physical process that requires further investigation using more closely collocated precipitation observations.

Overall, the results indicate that further improvements in the simulation of long-range Saharan dust transport should focus on two largely independent aspects. Meteorological initialization together with convection-permitting resolution substantially improves the timing, vertical distribution, and surface concentrations of transported dust. In contrast, the persistent coarse-particle deficit and associated optical discrepancies remain largely insensitive to these improvements and instead reflect limitations in the current aerosol representation. Future model development should therefore focus on improving the the representation of the emitted coarse-particle size distribution and size-dependent sedimentation and deposition processes and on extending the aerosol representation to include ageing and mixing processes that modify aerosol optical properties.

## 5 Conclusions

This study combined vertically resolved lidar observations, sun-photometer and in situ measurements, satellite products, backward trajectories, and ICON-ART simulations to investigate four contrasting Saharan dust events over southwestern Germany. The selected cases covered prolonged clear-sky transport, dust–cloud interactions, and an intense dust outbreak, providing a range of observational constraints on Saharan dust transport, vertical structure, optical properties, and boundary-layer entrainment.

ICON-ART reproduced the regional transport pathways and arrival of the Saharan air layers well, demonstrating that the model captures the synoptic-scale processes controlling long-range dust transport towards Western Europe. Separating the lidar-derived backscatter into dust and non-dust components enabled a consistent comparison with the modelled dust field and avoided attributing the contribution of other aerosols to model error. This separation provides an important constraint for evaluating dust transport in mixed aerosol layers.

The sensitivity experiments show that meteorological forcing and horizontal resolution play complementary roles. Daily reinitialization of the global simulation provided more accurate lateral boundary conditions and improved the timing and persistence of dust within the boundary layer. Convection-permitting simulations better represented layer stratification, vertical gradients, and exchange between the free troposphere and boundary layer, but their added value was realized only when the large-scale meteorological state and lateral boundary conditions were sufficiently accurate. Thus, higher resolution alone does not necessarily translate into a better dust forecast.

In contrast, persistent biases in particle size and associated optical properties were largely insensitive to meteorological initialization and grid spacing. ICON-ART shifted the transported dust towards smaller particle sizes, overestimating particles between approximately 0.5 and 2 $\mu$m while underestimating particles larger than 2 $\mu$m. The results therefore indicate that transport-related and aerosol-process errors are partly separable: improved meteorological forcing and resolution can improve plume timing and vertical redistribution, whereas the persistent coarse-particle deficit points to limitations in the representation of coarse-dust emissions and size-dependent removal processes.

Overall, the combination of vertically resolved and size-resolved observations provides a means of distinguishing dynamical from aerosol-process limitations in long-range dust simulations. Future model development should therefore prioritize the joint improvement of lateral meteorological forcing and coarse-dust process representation. This will require targeted evalu-

ation of coarse-particle emissions and removal processes together with more closely collocated observations of aerosol size, composition, clouds, and precipitation.

*Code availability.* The code used to analyse the lidar data is property of Raymetrics Inc, but we have shown that it generates the same results as the code single calculus chain (SCC) provided by EARLIENT https://www.earlinet.org/index.php?id=earlinet_homepage, last access: 8 March 2021). The ICON-ART model is open-source and accessible through https://zenodo.org/records/20762965

*Data availability.* The lidar raw data and in situ data are available via the open access data repository KIT open (doi will be added). Sun photometer data are available from the AErosol RObotic NETwork (Aeronet) data center at https://aeronet.gsfc.nasa.gov/ (last access: 22 October 2025). ICON-ART model simulation results are available upon request from the data originator (DWD; datenservice@dwd.de).

*Author contributions.* FW, HS, and HZ performed the measurements. GAH, HV, JF conducted the model simulations and post processing of the outputs. PS performed the high-resolution simulations and post-processing of model and satellite datasets. HZ and FW analysed the remote sensing data. HZ did write the manuscript with support from FW and HS as well as contributions from all co-authors.

*Competing interests.* At least one of the (co-)authors is a member of the editorial board of Atmospheric Chemistry and Physics.

*Acknowledgements.* Support by the staff of the Institute of Meteorology and Climate Research, and support by the project Modular Observation Solutions for Earth Systems (MOSES) of the Helmholtz Association (HGF). This work contributes to and is partly funded by the GLObal-to-Regional ICON Digital Twin (GLORI) project.

## References


Adebiyi, A. A. and Kok, J. F.: Climate models miss most of the coarse dust in the atmosphere, Science Advances, 6, eaaz9507, https://doi.org/10.1126/sciadv.aaz9507, 2020.

Ansmann, A., Bösenberg, J., Chaikovsky, A., Comerón, A., Eckhardt, S., Eixmann, R., Freudenthaler, V., Ginoux, P., Komguem, L., Linné, H., Márquez, M. L., Matthias, V., Mattis, I., Mitev, V., Müller, D., Music, S., Nickovic, S., Pelon, J., Sauvage, L., Sobolewsky, P., Srivastava, M. K., Stohl, A., Torres, O., Vaughan, G., Wandinger, U., and Wiegner, M.: Long-range transport of Saharan dust to northern Europe: The 11–16 October 2001 outbreak observed with EARLINET, Journal of Geophysical Research: Atmospheres, 108, https://doi.org/10.1029/2003JD003757, 2003.

Avdikos, G.: Powerful Raman Lidar systems for atmospheric analysis and high-energy physics experiments, EPJ Web of Conferences, 89, 04 003, https://doi.org/10.1051/epjconf/20158904003, publisher: EDP Sciences, 2015.

Barnaba, F. and Gobbi, G. P.: Aerosol seasonal variability over the Mediterranean region and relative impact of maritime, continental and Saharan dust particles over the basin from MODIS data in the year 2001, Atmospheric Chemistry and Physics, 4, 2367–2391, https://doi.org/10.5194/acp-4-2367-2004, publisher: Copernicus GmbH, 2004.

Benincasa, F.: Forecast comparison — WMO SDS-WAS, https://sds-was.aemet.es/forecast-products/dust-forecasts/forecast-comparison, 2023.

Cao, C., Zheng, S., and Singh, R. P.: Characteristics of aerosol optical properties and meteorological parameters during three major dust events (2005–2010) over Beijing, China, Atmospheric Research, 150, 129–142, https://doi.org/10.1016/j.atmosres.2014.07.022, 2014.

Chapman, E. G., Gustafson, W. I. J., Easter, R. C., Barnard, J. C., Ghan, S. J., Pekour, M. S., and Fast, J. D.: Coupling aerosol-cloud-radiative processes in the WRF-Chem model: Investigating the radiative impact of elevated point sources, Atmospheric Chemistry and Physics, 9, 945–964, https://doi.org/10.5194/acp-9-945-2009, publisher: Copernicus GmbH, 2009.

Chouza, F., Reitebuch, O., Benedetti, A., and Weinzierl, B.: Saharan dust long-range transport across the Atlantic studied by an airborne Doppler wind lidar and the MACC model, Atmospheric Chemistry and Physics, 16, 11 581–11 600, https://doi.org/10.5194/acp-16-11581-2016, publisher: Copernicus GmbH, 2016.

Conceição, R., Silva, H. G., Mirão, J., Gostein, M., Fialho, L., Narvarte, L., and Collares-Pereira, M.: Saharan dust transport to Europe and its impact on photovoltaic performance: A case study of soiling in Portugal, Solar Energy, 160, 94–102, https://doi.org/10.1016/j.solener.2017.11.059, 2018.

Diop, D., Niang, D. N., Drame, M. S., and Ba, A.: Dust Source, Vertical Profile and Climate Impact by RegCM3 Regional Climate Model over West Africa during 2006, Atmospheric and Climate Sciences, 10, 206–219, https://doi.org/10.4236/acs.2020.102011, number: 2 Publisher: Scientific Research Publishing, 2020.

Dubovik, O. and King, M. D.: A flexible inversion algorithm for retrieval of aerosol optical properties from Sun and sky radiance measurements, Journal of Geophysical Research: Atmospheres, 105, 20 673–20 696, https://doi.org/10.1029/2000JD900282, _eprint: https://onlinelibrary.wiley.com/doi/pdf/10.1029/2000JD900282, 2000.

Freudenthaler, V.: About the effects of polarising optics on lidar signals and the Δ90 calibration, Atmospheric Measurement Techniques, 9, 4181–4255, https://doi.org/10.5194/amt-9-4181-2016, publisher: Copernicus GmbH, 2016.

Freudenthaler, V., Esselborn, M., Wiegner, M., Heese, B., Tesche, M., Ansmann, A., Müller, D., Althausen, D., Wirth, M., Fix, A., Ehret, G., Knippertz, P., Toledano, C., Gasteiger, J., Garhammer, M., and Seefeldner, M.: Depolarization ratio profiling at several wave-

lengths in pure Saharan dust during SAMUM 2006, Tellus B, 61, 165–179, https://doi.org/10.1111/j.1600-0889.2008.00396.x, _eprint: https://onlinelibrary.wiley.com/doi/pdf/10.1111/j.1600-0889.2008.00396.x, 2009.

Gasteiger, J., Wiegner, M., Groß, S., Freudenthaler, V., Toledano, C., Tesche, M., and Kandler, K.: Modelling lidar-relevant optical properties of complex mineral dust aerosols, Tellus B: Chemical and Physical Meteorology, 63, 725–741, https://doi.org/10.1111/j.1600-0889.2011.00559.x, 2011.

Giles, D. M., Sinyuk, A., Sorokin, M. G., Schafer, J. S., Smirnov, A., Slutsker, I., Eck, T. F., Holben, B. N., Lewis, J. R., Campbell, J. R., Welton, E. J., Korkin, S. V., and Lyapustin, A. I.: Advancements in the Aerosol Robotic Network (AERONET) Version 3 database – automated near-real-time quality control algorithm with improved cloud screening for Sun photometer aerosol optical depth (AOD) measurements, Atmospheric Measurement Techniques, 12, 169–209, https://doi.org/10.5194/amt-12-169-2019, publisher: Copernicus GmbH, 2019.

GROß, S., TESCHE, M., FREUDENTHALER, V., TOLEDANO, C., WIEGNER, M., ANSMANN, A., ALTHAUSEN, D., and SEEFELDNER, M.: Characterization of Saharan dust, marine aerosols and mixtures of biomass-burning aerosols and dust by means of multi-wavelength depolarization and Raman lidar measurements during SAMUM 2, Tellus B, 63, 706–724, https://doi.org/https://doi.org/10.1111/j.1600-0889.2011.00556.x, 2011.

Guerzoni, S. and Chester, R., eds.: The Impact of Desert Dust Across the Mediterranean, vol. 11 of *Environmental Science and Technology Library*, Springer Netherlands, Dordrecht, https://doi.org/10.1007/978-94-017-3354-0, 1996.

Hermes, K., Quinting, J., Grams, C. M., Hoose, C., and Hoshyaripour, G. A.: Impact of Saharan dust outbreaks on short-range weather forecast errors in Europe, Quarterly Journal of the Royal Meteorological Society, 150, 1704–1723, https://doi.org/https://doi.org/10.1002/qj.4666, 2024.

Holben, B. N., Eck, T. F., Slutsker, I., Tanré, D., Buis, J. P., Setzer, A., Vermote, E., Reagan, J. A., Kaufman, Y. J., Nakajima, T., Lavenu, F., Jankowiak, I., and Smirnov, A.: AERONET - A federated instrument network and data archive for aerosol characterization, Remote Sensing of Environment, 66, 1–16, https://doi.org/10.1016/S0034-4257(98)00031-5, 1998.

Hoshyaripour, G. A., Bachmann, V., Förstner, J., Steiner, A., Vogel, H., Wagner, F., Walter, C., and Vogel, B.: Effects of Particle Nonsphericity on Dust Optical Properties in a Forecast System: Implications for Model-Observation Comparison, Journal of Geophysical Research: Atmospheres, 124, 7164–7178, https://doi.org/10.1029/2018JD030228, _eprint: https://onlinelibrary.wiley.com/doi/pdf/10.1029/2018JD030228, 2019.

Hoshyaripour, G. A., Baer, A., Bierbauer, S., Bruckert, J., Brunner, D., Förstner, J., Hamzehloo, A., Hanft, V., Keller, C., Klose, M., Kumar, P., Ludwig, P., Metzner, E., Muth, L., Pauling, A., Porz, N., Ramezani Ziarani, M., Reddmann, T., Reißig, L., Ruhnke, R., Satitkovitchai, K., Seifert, A., Sinnhuber, M., Steiner, M., Versick, S., Vogel, H., Weimer, M., Werchner, S., and Hoose, C.: The atmospheric composition component of the ICON modeling framework: ICON-ART version 2025.10, Geoscientific Model Development, 19, 1645–1681, https://doi.org/10.5194/gmd-19-1645-2026, 2026.

Jiang, F., Saathoff, H., Ezenobi, U., Song, J., Zhang, H., Gao, L., and Leisner, T.: Measurement report: Brown carbon aerosol in rural Germany – sources, chemistry, and diurnal variations, Atmospheric Chemistry and Physics, 25, 1917–1930, https://doi.org/10.5194/acp-25-1917-2025, 2025.

Jöckel, P., Tost, H., Pozzer, A., Brühl, C., Buchholz, J., Ganzeveld, L., Hoor, P., Kerkweg, A., Lawrence, M. G., Sander, R., Steil, B., Stiller, G., Tanarhte, M., Taraborrelli, D., van Aardenne, J., and Lelieveld, J.: The atmospheric chemistry general circulation model ECHAM5/MESSy1: consistent simulation of ozone from the surface to the mesosphere, Atmospheric Chemistry and Physics, 6, 5067–5104, https://doi.org/10.5194/acp-6-5067-2006, publisher: Copernicus GmbH, 2006.

Jöckel, P., Kerkweg, A., Pozzer, A., Sander, R., Tost, H., Riede, H., Baumgaertner, A., Gromov, S., and Kern, B.: Development cycle 2 of the Modular Earth Submodel System (MESSy2), Geoscientific Model Development, 3, 717–752, https://doi.org/10.5194/gmd-3-717-2010, publisher: Copernicus GmbH, 2010.

Kandler, K., Benker, N., Bundke, U., Cuevas, E., Ebert, M., Knippertz, P., Rodríguez, S., Schütz, L., and Weinbruch, S.: Chemical composition and complex refractive index of Saharan Mineral Dust at Izaña, Tenerife (Spain) derived by electron microscopy, Atmospheric Environment, 41, 8058–8074, https://doi.org/10.1016/j.atmosenv.2007.06.047, 2007.

Kanngießer, F. and Fiedler, S.: Intercomparison case study of data-driven reconstructions of a cloud-obscured Saharan dust plume in Europe, Scientific Reports, 16, 17 165, https://doi.org/10.1038/s41598-026-55422-y, 2026.

Kim, D., Chin, M., Yu, H., Eck, T. F., Sinyuk, A., Smirnov, A., and Holben, B. N.: Dust optical properties over North Africa and Arabian Peninsula derived from the AERONET dataset, Atmospheric Chemistry and Physics, 11, 10 733–10 741, https://doi.org/10.5194/acp-11-10733-2011, publisher: Copernicus GmbH, 2011.

Kunz, A., Pan, L. L., Konopka, P., Kinnison, D. E., and Tilmes, S.: Chemical and dynamical discontinuity at the extratropical tropopause based on START08 and WACCM analyses, Journal of Geophysical Research: Atmospheres, 116, https://doi.org/10.1029/2011JD016686, _eprint: https://onlinelibrary.wiley.com/doi/pdf/10.1029/2011JD016686, 2011.

Kunz, M., Abbas, S. S., Bauckholt, M., Böhmländer, A., Feuerle, T., Gasch, P., Glaser, C., Groß, J., Hajnsek, I., Handwerker, J., Hase, F., Khordakova, D., Knippertz, P., Kohler, M., Lange, D., Latt, M., Laube, J., Martin, L., Mauder, M., Möhler, O., Mohr, S., Reitter, R. W., Rettenmeier, A., Rolf, C., Saathoff, H., Schrön, M., Schütze, C., Spahr, S., Späth, F., Vogel, F., Völksch, I., Weber, U., Wieser, A., Wilhelm, J., Zhang, H., and Dietrich, P.: Swabian MOSES 2021: An interdisciplinary field campaign for investigating convective storms and their event chains, Frontiers in Earth Science, Volume 10 - 2022, https://doi.org/10.3389/feart.2022.999593, 2022a.

Kunz, M., Abbas, S. S., Bauckholt, M., Böhmländer, A., Feuerle, T., Gasch, P., Glaser, C., Groß, J., Hajnsek, I., Handwerker, J., Hase, F., Khordakova, D., Knippertz, P., Kohler, M., Lange, D., Latt, M., Laube, J., Martin, L., Mauder, M., Möhler, O., Mohr, S., Reitter, R. W., Rettenmeier, A., Rolf, C., Saathoff, H., Schrön, M., Schütze, C., Spahr, S., Späth, F., Vogel, F., Völksch, I., Weber, U., Wieser, A., Wilhelm, J., Zhang, H., and Dietrich, P.: Swabian MOSES 2021: An interdisciplinary field campaign for investigating convective storms and their event chains, Frontiers in Earth Science, 10, https://www.frontiersin.org/articles/10.3389/feart.2022.999593, 2022b.

Liu, Z., Omar, A., Vaughan, M., Hair, J., Kittaka, C., Hu, Y., Powell, K., Trepte, C., Winker, D., Hostetler, C., Ferrare, R., and Pierce, R.: CALIPSO lidar observations of the optical properties of Saharan dust: A case study of long-range transport, Journal of Geophysical Research: Atmospheres, 113, https://doi.org/10.1029/2007JD008878, _eprint: https://onlinelibrary.wiley.com/doi/pdf/10.1029/2007JD008878, 2008.

Mallet, M., Tulet, P., Serça, D., Solmon, F., Dubovik, O., Pelon, J., Pont, V., and Thouron, O.: Impact of dust aerosols on the radiative budget, surface heat fluxes, heating rate profiles and convective activity over West Africa during March 2006, Atmospheric Chemistry and Physics, 9, 7143–7160, https://doi.org/10.5194/acp-9-7143-2009, publisher: Copernicus GmbH, 2009.

Merdji, A. B., Lu, C., Xu, X., and Mhawish, A.: Long-term three-dimensional distribution and transport of Saharan dust: Observation from CALIPSO, MODIS, and reanalysis data, Atmospheric Research, 286, 106 658, https://doi.org/10.1016/j.atmosres.2023.106658, 2023.

Middleton, N. J. and Goudie, A. S.: Saharan dust: sources and trajectories, Transactions of the Institute of British Geographers, 26, 165–181, https://doi.org/10.1111/1475-5661.00013, _eprint: https://onlinelibrary.wiley.com/doi/pdf/10.1111/1475-5661.00013, 2001.

Misra, A., Tripathi, S. N., Kaul, D. S., and Welton, E. J.: Study of MPLNET-Derived Aerosol Climatology over Kanpur, India, and Validation of CALIPSO Level 2 Version 3 Backscatter and Extinction Products, Journal of Atmospheric and Oceanic Technology, 29, 1285–1294,

https://doi.org/10.1175/JTECH-D-11-00162.1, publisher: American Meteorological Society Section: Journal of Atmospheric and Oceanic Technology, 2012.

Molinaroli, E., Guerzoni, S., and Rampazzo, G.: Contribution of Saharan dust to the Central Mediterranean Basin, in: Processes Controlling the Composition of Clastic Sediments, edited by Johnsson, M. J. and Basu, A., vol. 284, p. 0, Geological Society of America, https://doi.org/10.1130/SPE284-p303, 1993.

Mona, L., Papagiannopoulos, N., Basart, S., Baldasano, J., Binietoglou, I., Cornacchia, C., and Pappalardo, G.: EARLINET dust observations vs. BSC-DREAM8b modeled profiles: 12-year-long systematic comparison at Potenza, Italy, Atmospheric Chemistry and Physics, 14, 8781–8793, https://doi.org/10.5194/acp-14-8781-2014, publisher: Copernicus GmbH, 2014.

Müller, D., Weinzierl, B., Petzold, A., Kandler, K., Ansmann, A., Müller, T., Tesche, M., Freudenthaler, V., Esselborn, M., Heese, B., Althausen, D., Schladitz, A., Otto, S., and Knippertz, P.: Mineral dust observed with AERONET Sun photometer, Raman lidar, and in situ instruments during SAMUM 2006: Shape-independent particle properties, Journal of Geophysical Research: Atmospheres, 115, https://doi.org/10.1029/2009JD012520, _eprint: https://onlinelibrary.wiley.com/doi/pdf/10.1029/2009JD012520, 2010.

Pozzoli, L., Bey, I., Rast, S., Schultz, M. G., Stier, P., and Feichter, J.: Trace gas and aerosol interactions in the fully coupled model of aerosol-chemistry-climate ECHAM5-HAMMOZ: 1. Model description and insights from the spring 2001 TRACE-P experiment, Journal of Geophysical Research: Atmospheres, 113, https://doi.org/10.1029/2007JD009007, _eprint: https://onlinelibrary.wiley.com/doi/pdf/10.1029/2007JD009007, 2008a.

Pozzoli, L., Bey, I., Rast, S., Schultz, M. G., Stier, P., and Feichter, J.: Trace gas and aerosol interactions in the fully coupled model of aerosol-chemistry-climate ECHAM5-HAMMOZ: 2. Impact of heterogeneous chemistry on the global aerosol distributions, Journal of Geophysical Research: Atmospheres, 113, https://doi.org/10.1029/2007JD009008, _eprint: https://onlinelibrary.wiley.com/doi/pdf/10.1029/2007JD009008, 2008b.

Ratcliffe, N. G., Ryder, C. L., Bellouin, N., Jones, A., Johnson, B., Woodward, S., Wieland, L.-M., Gasteiger, J., and Weinzierl, B.: New processes to counteract sedimentation of coarse dust particles are required for climate models to agree with aircraft observations, EGUsphere, 2025, 1–33, https://doi.org/10.5194/egusphere-2025-5143, 2025.

Rieger, D., Bangert, M., Bischoff-Gauss, I., Förstner, J., Lundgren, K., Reinert, D., Schröter, J., Vogel, H., Zängl, G., Ruhnke, R., and Vogel, B.: ICON–ART 1.0 – a new online-coupled model system from the global to regional scale, Geoscientific Model Development, 8, 1659–1676, https://doi.org/10.5194/gmd-8-1659-2015, 2015.

Rieger, D., Steiner, A., Bachmann, V., Gasch, P., Förstner, J., Deetz, K., Vogel, B., and Vogel, H.: Impact of the 4 April 2014 Saharan dust outbreak on the photovoltaic power generation in Germany, Atmospheric Chemistry and Physics, 17, 13 391–13 415, https://doi.org/10.5194/acp-17-13391-2017, 2017a.

Rieger, D., Steiner, A., Bachmann, V., Gasch, P., Förstner, J., Deetz, K., Vogel, B., and Vogel, H.: Impact of the 4 April 2014 Saharan dust outbreak on the photovoltaic power generation in Germany, Atmospheric Chemistry and Physics, 17, 13 391–13 415, https://doi.org/10.5194/acp-17-13391-2017, publisher: Copernicus GmbH, 2017b.

Roeckner, E., Brokopf, R., Esch, M., Giorgetta, M., Hagemann, S., Kornblueh, L., Manzini, E., Schlese, U., and Schulzweida, U.: Sensitivity of Simulated Climate to Horizontal and Vertical Resolution in the ECHAM5 Atmosphere Model, Journal of Climate, 19, 3771–3791, https://doi.org/10.1175/JCLI3824.1, publisher: American Meteorological Society Section: Journal of Climate, 2006.

Rostási, , Topa, B. A., Gresina, F., Weiszburg, T. G., Gelencsér, A., and Varga, G.: Saharan Dust Deposition in Central Europe in 2016—A Representative Year of the Increased North African Dust Removal Over the Last Decade, Frontiers in Earth Science, 10, https://www.frontiersin.org/articles/10.3389/feart.2022.869902, 2022.

Saidou Chaibou, A. A., Ma, X., and Sha, T.: Dust radiative forcing and its impact on surface energy budget over West Africa, Scientific Reports, 10, 12 236, https://doi.org/10.1038/s41598-020-69223-4, number: 1 Publisher: Nature Publishing Group, 2020.

Schuster, G. L., Vaughan, M., MacDonnell, D., Su, W., Winker, D., Dubovik, O., Lapyonok, T., and Trepte, C.: Comparison of CALIPSO aerosol optical depth retrievals to AERONET measurements, and a climatology for the lidar ratio of dust, Atmospheric Chemistry and Physics, 12, 7431–7452, https://doi.org/10.5194/acp-12-7431-2012, publisher: Copernicus GmbH, 2012.

Seifert, A., Bachmann, V., Filipitsch, F., Förstner, J., Grams, C. M., Hoshyaripour, G. A., Quinting, J., Rohde, A., Vogel, H., Wagner, A., and Vogel, B.: Aerosol–cloud–radiation interaction during Saharan dust episodes: the dusty cirrus puzzle, Atmospheric Chemistry and Physics, 23, 6409–6430, https://doi.org/10.5194/acp-23-6409-2023, 2023.

Sinyuk, A., Holben, B. N., Eck, T. F., Giles, D. M., Slutsker, I., Korkin, S., Schafer, J. S., Smirnov, A., Sorokin, M., and Lyapustin, A.: The AERONET Version 3 aerosol retrieval algorithm, associated uncertainties and comparisons to Version 2, Atmospheric Measurement Techniques, 13, 3375–3411, https://doi.org/10.5194/amt-13-3375-2020, publisher: Copernicus GmbH, 2020.

Smith, K., Garcia, R., Marsh, D., and Richter, H.: WACCM simulations of the mean circulation and trace species transport in the winter mesosphere, Journal of Geophysical Research-Atmospheres, https://doi.org/10.1029/2011JD016083, 2011.

Song, Q., Zhang, Z., Yu, H., Kok, J. F., Di Biagio, C., Albani, S., Zheng, J., and Ding, J.: Size-resolved dust direct radiative effect efficiency derived from satellite observations, Atmospheric Chemistry and Physics, 22, 13 115–13 135, https://doi.org/10.5194/acp-22-13115-2022, publisher: Copernicus GmbH, 2022.

Sugimoto, N., Nishizawa, T., Shimizu, A., and Jin, Y.: The Asian Dust and Aerosol Lidar Observation Network (AD-Net), in: Light, Energy and the Environment (2016), paper EW2A.1, p. EW2A.1, Optica Publishing Group, https://doi.org/10.1364/EE.2016.EW2A.1, 2016.

Tanaka, T. Y., Kurosaki, Y., Chiba, M., Matsumura, T., Nagai, T., Yamazaki, A., Uchiyama, A., Tsunematsu, N., and Kai, K.: Possible transcontinental dust transport from North Africa and the Middle East to East Asia, Atmospheric Environment, 39, 3901–3909, https://doi.org/10.1016/j.atmosenv.2005.03.034, 2005.

Tesche, M., Ansmann, A., Müller, D., Althausen, D., Engelmann, R., Freudenthaler, V., and Groß, S.: Vertically resolved separation of dust and smoke over Cape Verde using multiwavelength Raman and polarization lidars during Saharan Mineral Dust Experiment 2008, Journal of Geophysical Research: Atmospheres, 114, https://doi.org/https://doi.org/10.1029/2009JD011862, 2009a.

Tesche, M., Ansmann, A., Müller, D., Althausen, D., Engelmann, R., Freudenthaler, V., and Groß, S.: Vertically resolved separation of dust and smoke over Cape Verde using multiwavelength Raman and polarization lidars during Saharan Mineral Dust Experiment 2008, Journal of Geophysical Research: Atmospheres, 114, https://doi.org/10.1029/2009JD011862, _eprint: https://onlinelibrary.wiley.com/doi/pdf/10.1029/2009JD011862, 2009b.

Varga, G.: Changing nature of Saharan dust deposition in the Carpathian Basin (Central Europe): 40 years of identified North African dust events (1979–2018), Environment International, 139, 105 712, https://doi.org/10.1016/j.envint.2020.105712, 2020.

Vermeulen, A., Devaux, C., and Herman, M.: Retrieval of the scattering and microphysical properties of aerosols from ground-based optical measurements including polarization. I. Method, Applied Optics, 39, 6207–6220, https://doi.org/10.1364/AO.39.006207, publisher: Optica Publishing Group, 2000.

Vogel, B., Hoose, C., Vogel, H., and Kottmeier, C.: A model of dust transport applied to the Dead Sea Area, Meteorologische Zeitschrift, pp. 611–624, https://doi.org/10.1127/0941-2948/2006/0168, publisher: Schweizerbart'sche Verlagsbuchhandlung, 2006.

Vogel, H., Förstner, J., Vogel, B., Hanisch, T., Mühr, B., Schättler, U., and Schad, T.: Time-lagged ensemble simulations of the dispersion of the Eyjafjallajökull plume over Europe with COSMO-ART, Atmospheric Chemistry and Physics, 14, 7837–7845, https://doi.org/10.5194/acp-14-7837-2014, publisher: Copernicus GmbH, 2014.

Weimer, M., Schröter, J., Eckstein, J., Deetz, K., Neumaier, M., Fischbeck, G., Hu, L., Millet, D. B., Rieger, D., Vogel, H., Vogel, B., Reddmann, T., Kirner, O., Ruhnke, R., and Braesicke, P.: An emission module for ICON-ART 2.0: implementation and simulations of acetone, Geoscientific Model Development, 10, 2471–2494, https://doi.org/10.5194/gmd-10-2471-2017, publisher: Copernicus GmbH, 2017.

Wu, M., Liu, X., Yu, H., Wang, H., Shi, Y., Yang, K., Darmenov, A., Wu, C., Wang, Z., Luo, T., Feng, Y., and Ke, Z.: Understanding processes that control dust spatial distributions with global climate models and satellite observations, Atmospheric Chemistry and Physics, 20, 13 835–13 855, https://doi.org/10.5194/acp-20-13835-2020, publisher: Copernicus GmbH, 2020.

Zhang, H., Wagner, F., Saathoff, H., Vogel, H., Hoshyaripour, G., Bachmann, V., Förstner, J., and Leisner, T.: Comparison of Scanning LiDAR with Other Remote Sensing Measurements and Transport Model Predictions for a Saharan Dust Case, Remote Sensing, 14, 1693, https://doi.org/10.3390/rs14071693, number: 7 Publisher: Multidisciplinary Digital Publishing Institute, 2022.

Zängl, G., Reinert, D., Rípodas, P., and Baldauf, M.: The ICON (ICOsahedral Non-hydrostatic) modelling framework of DWD and MPI-M: Description of the non-hydrostatic dynamical core, Quarterly Journal of the Royal Meteorological Society, 141, 563–579, https://doi.org/10.1002/qj.2378, _eprint: https://onlinelibrary.wiley.com/doi/pdf/10.1002/qj.2378, 2015.